Monthly Notices
of the
ROYAL ASTRONOMICAL SOCIETY

Mon. Not. R. Astron. Soc. **423,** 1503–1520 (2012) doi:10.1111/j.1365-2966.2012.20973.x

Rossiter–McLaughlin effect measurements for WASP-16, WASP-25 and WASP-31⋆

D. J. A. Brown,[1]† A. Collier Cameron,[1] D. R. Anderson,[2] B. Enoch,[1] C. Hellier,[2] P. F. L. Maxted,[2] G. R. M. Miller,[1] D. Pollacco,[3] D. Queloz,[4] E. Simpson,[3] B. Smalley,[2] A. H. M. J. Triaud,[4] I. Boisse,[5] F. Bouchy,[6,7] M. Gillon[8] and G. Hébrard[6,7]

[1]*SUPA, School of Physics and Astronomy, University of St Andrews, North Haugh, St Andrews, Fife KY16 9SS*
[2]*Astrophysics Group, School of Chemistry and Physics, Keele University, Staffordshire ST5 5BG*
[3]*Astrophysics Research Centre, School of Mathematics & Physics, Queen's University, University Road, Belfast BT7 1NN*
[4]*Observatoire Astronomique de l'Université de Genève, Chemin des Maillettes 51, CH-1290 Sauverny, Switzerland*
[5]*Centro de Astrofisica da Universidade do Porto, Rua das Estrelas, 4150-762 Porto, Portugal*
[6]*Institut d'Astrophysique de Paris, UMR7095 CNRS, Université Pierre & Marie Curie, 98bis Boulevard Arago, 75014 Paris, France*
[7]*Observatoire de Haute Provence, CNRS/OAMP, 04870 St Michel l'Observatoire, France*
[8]*Institut d'Astrophysique et de Géophysique, Université de Liège, Allée du 6 Août 17, Bat. B5C, Liége 1, Belgium*

Accepted 2012 March 21. Received 2012 March 16; in original form 2011 August 26

ABSTRACT

We present new measurements of the Rossiter–McLaughlin (RM) effect for three Wide Angle Search for transiting Planets (WASP) planetary systems, WASP-16, WASP-25 and WASP-31, from a combined analysis of their complete sets of photometric and spectroscopic data. We find a low-amplitude RM effect for WASP-16 ($T_{\rm eff} = 5700 \pm 150$ K), suggesting that the star is a slow rotator and thus of an advanced age, and obtain a projected alignment angle of $\lambda = -4\overset{\circ}{.}2^{+11.0}_{-13.9}$. For WASP-25 ($T_{\rm eff} = 5750 \pm 100$ K), we detect a projected spin–orbit angle of $\lambda = 14\overset{\circ}{.}6 \pm 6\overset{\circ}{.}7$. WASP-31 ($T_{\rm eff} = 6300 \pm 100$ K) is found to be well aligned, with a projected spin–orbit angle of $\lambda = 2\overset{\circ}{.}8 \pm 3\overset{\circ}{.}1$. A circular orbit is consistent with the data for all three systems, in agreement with their respective discovery papers. We consider the results for these systems in the context of the ensemble of RM measurements made to date. We find that whilst WASP-16 fits the hypothesis of Winn et al. that 'cool' stars ($T_{\rm eff} < 6250$ K) are preferentially aligned, WASP-31 has little impact on the proposed trend. We bring the total distribution of the true spin–orbit alignment angle, ψ, up to date, noting that recent results have improved the agreement with the theory of Fabrycky & Tremaine at mid-range angles. We also suggest a new test for judging misalignment using the Bayesian information criterion, according to which WASP-25 b's orbit should be considered to be aligned.

Key words: techniques: radial velocities – stars: individual: WASP-16 – stars: individual: WASP-25 – stars: individual: WASP-31 – planetary systems.

1 INTRODUCTION

As the number of transiting 'hot Jupiters' known to astronomy has grown, there has been a gradually increasing push towards fully categorizing their physical and orbital properties. It is widely presumed that close-in gas giants do not form at the locations in which we observe them, and there are competing theories to describe the process that leads them to their observable orbits.

Migration induced by a protoplanetary disc provides one means by which such a situation can be explained (Lin, Bodenheimer & Richardson 1996). Since such discs are generally aligned with the host star owing to angular momentum conservation, we would expect that disc migration would preferentially produce well-aligned hot Jupiter systems. Some misaligned planets would not be out of place under this mechanism, being the result of close planet–planet encounters following migration, but we would expect the majority of planets to exhibit spin–orbit alignment.

The Kozai–Lidov mechanism (Kozai 1962; Lidov 1962) is the basis of a competing theory for which evidence is mounting. The presence of a third, outer body in a planetary system can excite

⋆ Based on observations made using the CORALIE high-resolution echelle spectrograph mounted on the 1.2-m Euler Swiss Telescope and the HARPS high-resolution echelle spectrograph mounted on the ESO 3.6-m (under proposals 084.C-0185 and 085.C-0393), both at the ESO La Silla observatory.
†E-mail: djab@st-andrews.ac.uk

periodic oscillations in both the eccentricity and inclination of a planetary orbit; inward migration then follows, with tidal friction kicking in as the planet approaches its host, causing the orbit to shrink and circularize (Fabrycky & Tremaine 2007). The oscillating inclination that results from Kozai–Lidov interactions produces a continuum of inclinations once the orbits are stable, and thus we would expect the majority of hot Jupiters to exhibit misaligned orbits if the Kozai–Lidov mechanism operates.

It is possible, to some extent, to distinguish between these competing theories through measurement of the spin–orbit alignment angles of hot Jupiter systems. Given the different angular distributions predicted by these theories, building up a significant number of spin-angle measurements is a useful means of determining which mechanism is acting. Unfortunately, the true misalignment angle cannot be measured unless a spectroscopic measurement of $v \sin I$ is made, and the stellar rotation period is known. This yields an estimate of the inclination axis to the line of sight (e.g. Schlaufman 2010). The situation is made more difficult by systematic uncertainties in $v \sin I$ measurements, and the sine function, which flattens as it approaches 90° and therefore only yields useful measurements at low to intermediate inclinations. We are thus currently limited to measuring the projected spin–orbit misalignment angle in the plane of the sky. This is generally measured through the Rossiter–McLaughlin (RM) effect (McLaughlin 1924; Rossiter 1924) which is observable during transit. As the planet transits the approaching limb of the star, its spectrum is redshifted, and when it transits the receding limb its spectrum is blueshifted. The precise form of the RM anomaly in the radial velocity (RV) curve gives the projected misalignment angle, λ.

The first observation of the RM effect for a transiting planet was made by Queloz et al. (2000a), and since then the number of measurements has increased significantly to a level such that it is possible to begin carrying out analysis of the ensemble of measurements. Fabrycky & Winn (2009) investigated 11 systems with known values of λ, deriving two theoretical distributions for ψ, the true misalignment angle, using different assumptions about the form of the distribution. They suggested, based on an apparent dual population within their data set, that there might be two routes for planet migration, one producing mostly aligned planets and the other producing misaligned planets.

One early indication of a pattern was that misaligned planets tended to be high mass and on eccentric orbits (Johnson et al. 2009). Subsequent observations have often countered this initial trend (for example HAT-P-7; Narita et al. 2009; Winn et al. 2009a), but high mass ($M_{\rm p} > 4\,M_{\rm Jup}$) planets do appear to have a different obliquity distribution (Hébrard et al. 2011b). Of the six planets in this category with measured misalignment angles, four are misaligned, but none has $|\lambda| > 50^\circ$. More observations of high-mass planets are needed before we can be certain that this is not merely an artefact of small-number statistics, however.

One of the more intriguing suggestions was put forward by Winn et al. (2010b, hereafter W10), who speculated that the division into aligned and misaligned planets might be dependent on the effective temperature of the host star. Using a larger sample of 19 systems with known λ, they found that the misaligned systems were preferentially hotter than the aligned examples, with a critical temperature of $T_{\rm eff} \approx 6250$ K dividing the two populations. One explanation put forward for this was the tidal realignment of planets around 'cool' stars, with the equivalent process around 'hot' stars being suppressed owing to their lack of a convective envelope. W10 further conjecture that the current ψ distribution could be completely explained by a migration mechanism driven by a combination of Kozai–Lidov oscillations and planet–planet scattering, without the need to invoke disc migration.

Triaud et al. (2010, hereafter T10) added six planets to the ensemble of known RM measurements. Calculating individual ψ distributions for each planet based on the assumption that stellar rotation axes are randomly oriented on the sky, they produced a total distribution for the ensemble of planets, finding that it matched the theoretical distribution of Fabrycky & Tremaine (2007) for Kozai–Lidov mechanism dominated migration, further implying that disc migration might be superfluous to requirements for explaining the presence of hot Jupiters.

Here we present measurements of the RM angle for three more planets from the Wide Angle Search for transiting Planets (WASP; Pollacco et al. 2006), WASP-16 b, WASP-25 b and WASP-31 b, and investigate how they modify the ensemble results and conclusions discussed above. In Section 2, we give details of our observations, and in Section 3 we discuss the analytical methods used to determine the misalignment angles. In Section 4, we report on the results of our analysis for the individual systems. In Section 5, we discuss the implications of our results for previously observed trends. Finally, in Section 6, we take another look at the question of alignment, presenting a new test for planetary orbit misalignment.

2 OBSERVATIONS

RV data for all three planetary systems were obtained using the CORALIE high-precision echelle spectrograph (Queloz et al. 2000b), mounted on the Swiss 1.2-m Euler telescope, and with the HARPS high-precision echelle spectrograph (Mayor et al. 2003) mounted on the 3.6-m European Southern Observatory (ESO) telescope at La Silla. Data from CORALIE were used primarily to constrain the presence of a long-term trend in RV that might be indicative of a third body in the system, whilst HARPS was used to monitor the RV before, during and after a specific transit event. Two data points were obtained the night before the transit, and for at least one night following the transit; on the night of the transit, observations were started 90 min prior to the predicted start of transit and continued until 90 min after its predicted conclusion.

2.1 WASP-16

WASP-16 was observed using CORALIE between 2008 March 10 and 2009 June 3, on an ad hoc basis. One datum was also acquired on 2010 July 14 to retest the hypothesis of a long-term RV trend. The transit observed with HARPS occurred on the night of 2010 March 21; 32 data points were acquired over the duration of the night. This transit observation was affected by cloud cover, so an additional transit was observed on the night of 2011 May 12, producing a further 28 RV measurements. Further measurements were made on the days surrounding this transit as well (see journal of observations, Tables B1–B3).

Details of the photometric observations of WASP-16 are given in Lister et al. (2009).

2.2 WASP-25

HARPS observed the transit taking place on the night of 2008 April 11. 44 observations were made that night, with additional data acquired on adjacent nights (see the journal of observations, Tables B4 and B5). The system was observed using CORALIE between 2008 December 29 and 2009 June 28, with observations made at irregular intervals between these dates.

Enoch et al. (2011) describe the photometric observations that were made of WASP-25.

2.3 WASP-31

WASP-31 was observed using CORALIE between 2009 January 4 and 2010 May 18 during several short runs. HARPS was used to observe a full transit on the night of 2010 April 15, with 17 data points obtained. Additional observations were made on adjacent nights (see the journal of observations, Tables B6 and B7).

The photometric observations for WASP-31 are discussed in Anderson et al. (2011b).

3 DATA ANALYSIS

Our analysis mirrors that of T10, using the complete set of photometric and spectroscopic data for the objects that we investigate in order to fully account for parameter correlations. We use an adapted version of the code described in Collier Cameron et al. (2007), fitting models of the photometric transit, the Keplerian RV and the RM effect to the system data. The fit of our model is refined using a Markov Chain Monte Carlo (MCMC) technique to minimize the χ^2 statistic, and to explore the parameter space using the jump parameters T_0 (epoch of mid-transit), P (orbital period), W (transit width), b (impact parameter), γ velocity, $\dot{\gamma}$, K (RV semi-amplitude), $T_{\rm eff}$ (stellar effective temperature), [Fe/H] (metallicity), $\sqrt{e}\cos\omega$, $\sqrt{e}\sin\omega$, $\sqrt{v\sin I}\cos\lambda$ and $\sqrt{v\sin I}\sin\lambda$. We use a burn-in phase of 2000 steps, with burn-in judged to be complete when χ^2 becomes greater than the median of all previous values (Knutson et al. 2008). A minimum burn-in length of 500 steps is applied to ensure that burn-in is truly complete. Once this initial phase is over we use a further 100 steps to recalculate the parameter jump lengths before beginning the real Markov Chain of 10 000 accepted steps; with the acceptance rate of 25 per cent recommended for the Metropolis–Hastings algorithm (Tegmark et al. 2004), this gives an effective chain length of 40 000 steps. Our set of final parameters is taken to be the median of the Markov chain, with the 1σ error bars calculated from the values that encompass the central 68.3 per cent of the accepted steps. We account for limb darkening using a non-linear treatment based on the tables of Claret (2000), interpolating the coefficients at each step in the chain.

The inclusion of the photometric data is an important point. Although we fit the RM effect to the RV data, the transit width and depth, as well as the impact parameter, can be determined from the photometric transit. These parameters have a role to play in the characterization of the form of the RM anomaly. The transit width helps in determining the duration of the anomaly, whilst the depth gives the planetary and stellar radii. The radii and impact parameter in turn help us to determine $v\sin I$, upon which the amplitude of the anomaly depends (Queloz et al. 2000a). Although characterization of the RM effect can be carried out using the spectroscopic data alone, by taking the photometric data into account in this way we ensure consistency across the full set of system parameters. To account for stellar jitter, we initially assign a value of $1\,{\rm m\,s^{-1}}$, below the level of precision of the spectrographs used for this work, which we added in quadrature to the in-transit photometric data.

We separate our RV data by instrument, and within those distinctions also treat spectroscopic data taken on nights featuring planetary transits as separate data sets. Our model for the orbital RV signature treats the sets of data as independent, producing individual offsets and RV trends for each one. The reported solution is that for the set of RV data covering the greatest phase range. For completeness, we also repeated our analysis using *only* RV data taken during nights that featured a transit event, but found little to distinguish them from our analysis of the full set of data.

For our RM model, we use the analytic formula of Hirano et al. (2011a). This method requires prior knowledge of several broadening coefficients, specifically the macroturbulence, for which our estimates are noted in Table 1, and the Lorentzian (γ) and Gaussian (β) spectral line dispersions. The line dispersions were dictated by our use of the HARPS instrument, which has a spectral resolution of $R = 115\,000$, implying an instrumental Gaussian dispersion of $2.61\,{\rm km\,s^{-1}}$. This was combined with the intrinsic Doppler linewidth, including appropriate thermal and turbulent motion for each star, to obtain values of $\beta = 3.1\,{\rm km\,s^{-1}}$ for WASP-16 and WASP-25, and $\beta = 3.3\,{\rm km\,s^{-1}}$ for WASP-31. We assumed $\gamma = 0.9\,{\rm km\,s^{-1}}$ in line with Hirano et al., and also assumed that the coefficient of differential rotation $\alpha = 0$. WASP-16 and WASP-25 are both slow rotators, and whilst WASP-31 should be considered a moderately fast rotator, without knowledge of the inclination of the stellar rotation axis it is difficult to place a value of α.

We apply several Bayesian priors to χ^2 to account for previously known information: a prior on the eccentricity, allowing for the forcing of circular solutions; a prior on the spectroscopic $v\sin I$, using updated values of $v\sin I$ derived from the newly acquired

Table 1. System parameters for the three WASP planetary systems for which we evaluate the Rossiter–McLaughlin effect. Parameters for WASP-16 were taken from Lister et al. (2009). Parameters for WASP-25 were taken from Enoch et al. (2011). Parameters for WASP-31 were taken from Anderson et al. (2011b). $v\sin I$ and macroturbulence values have been updated through spectroscopic analysis of the new HARPS data using the Bruntt et al. (2010) calibration.

Parameter	Unit	WASP-16	WASP-25	WASP-31
M_*	$M_\odot$	$1.022^{+0.074}_{-0.129}$	1.00 ± 0.03	1.161 ± 0.026
R_*	$R_\odot$	$0.946^{+0.057}_{-0.052}$	0.92 ± 0.04	1.241 ± 0.039
$T_{\rm eff}$	K	5700 ± 150	5750 ± 100	6300 ± 100
$v\sin I$	${\rm km\,s^{-1}}$	2.3 ± 0.4	2.6 ± 0.4	8.1 ± 0.5
Macroturbulence	${\rm km\,s^{-1}}$	2.3	2.4	4.2
$M_{\rm p}$	$M_{\rm Jup}$	$0.855^{+0.043}_{-0.076}$	0.58 ± 0.04	0.478 ± 0.030
$R_{\rm p}$	$R_{\rm Jup}$	$1.008^{+0.083}_{-0.060}$	$1.22^{+0.06}_{-0.05}$	1.537 ± 0.060
P	d	$3.118\,60 \pm 0.000\,01$	$3.764\,825 \pm 0.000\,005$	$3.405\,909 \pm 0.000\,005$
a	au	$0.0421^{+0.0010}_{-0.0019}$	0.0473 ± 0.0004	$0.046\,57 \pm 0.000\,34$
e		0 (adopted)	0 (adopted)	0 (adopted)
i	$^\circ$	$85.22^{+0.27}_{-0.43}$	88.0 ± 0.5	84.54 ± 0.27

Table 2. A comparison of the χ^2 and $\chi^2_{\rm red}$ values for WASP-16 for each combination of Bayesian priors. All values of χ^2 include the Bayesian penalties applicable for that combination of priors.

$v \sin I$ prior	MS prior	$\dot{\gamma}$ ($\rm ms^{-1}yr^{-1}$)	Eccentricity	$v \sin I$ ($\rm km\,s^{-1}$)	λ (°)	χ^2	$\chi^2_{\rm RV}$	$\chi^2_{\rm red}$
Off	Off	0	$0.009^{+0.010}_{-0.006}$	1.2 ± 0.4	$-2.1^{+10.5}_{-11.0}$	$12\,915 \pm 161$	100 ± 14	0.9 ± 0.1
Off	On	0	$0.004^{+0.006}_{-0.002}$	$1.2^{+0.4}_{-0.5}$	$-2.8^{+10.7}_{-11.1}$	$12\,917 \pm 161$	102 ± 14	0.9 ± 0.1
Off	Off	$1.0^{+0.8}_{-0.8}$	$0.011^{+0.009}_{-0.007}$	$1.0^{+0.5}_{-0.6}$	$-2.5^{+13.6}_{-16.6}$	$12\,912 \pm 161$	99 ± 14	0.9 ± 0.1
Off	On	$0.6^{+0.5}_{-0.3}$	$0.007^{+0.007}_{-0.005}$	$1.1^{+0.4}_{-0.6}$	$-3.6^{+10.9}_{-14.8}$	$12\,911 \pm 161$	99 ± 14	0.9 ± 0.1
Off	Off	0	0	$1.1^{+0.5}_{-0.6}$	$-6.7^{+11.7}_{-19.2}$	$12\,917 \pm 161$	103 ± 14	1.0 ± 0.1
Off	On	0	0	$1.2^{+0.4}_{-0.5}$	$-4.2^{+11.0}_{-13.9}$	$12\,916 \pm 161$	103 ± 14	1.0 ± 0.1
Off	Off	0.1 ± 0.1	0	$1.1^{+0.5}_{-0.6}$	$-5.8^{+10.6}_{-14.5}$	$12\,917 \pm 161$	102 ± 14	0.9 ± 0.1
Off	On	$0.9^{+1.0}_{-0.9}$	0	1.2 ± 0.5	$-6.0^{+10.3}_{-15.4}$	$12\,911 \pm 161$	102 ± 14	0.9 ± 0.1
2.3 ± 0.4	Off	0	$0.011^{+0.009}_{-0.008}$	1.2 ± 0.3	$-1.8^{+11.0}_{-11.2}$	$12\,910 \pm 161$	100 ± 14	0.9 ± 0.1
2.3 ± 0.4	On	0	$0.012^{+0.009}_{-0.007}$	1.2 ± 0.2	$-2.3^{+10.5}_{-11.7}$	$12\,914 \pm 161$	98 ± 14	0.9 ± 0.1
2.3 ± 0.4	Off	0.1 ± 0.1	$0.010^{+0.009}_{-0.007}$	1.2 ± 0.3	$-3.6^{+11.7}_{-11.3}$	$12\,916 \pm 161$	101 ± 14	0.9 ± 0.1
2.3 ± 0.4	On	$0.7^{+0.7}_{-0.8}$	$0.011^{+0.009}_{-0.007}$	1.2 ± 0.2	$-2.9^{+9.9}_{-9.0}$	$12\,912 \pm 161$	99 ± 14	0.9 ± 0.1
2.3 ± 0.4	Off	0	0	1.2 ± 0.3	$-4.9^{+10.0}_{-11.0}$	$12\,912 \pm 161$	102 ± 14	0.9 ± 0.1
2.3 ± 0.4	On	0	0	1.2 ± 0.3	$-4.8^{+9.6}_{-10.2}$	$12\,919 \pm 161$	104 ± 14	1.0 ± 0.1
2.3 ± 0.4	Off	$2.1^{+3.3}_{-1.8}$	0	$1.1^{+0.3}_{-0.4}$	$-5.6^{+10.0}_{-12.9}$	$12\,916 \pm 161$	101 ± 14	0.9 ± 0.1
2.3 ± 0.4	On	$-0.6^{+1.6}_{-1.3}$	0	1.1 ± 0.4	$-5.7^{+11.4}_{-12.5}$	$12\,917 \pm 161$	103 ± 14	0.9 ± 0.1

HARPS spectra and the macroturbulence calibration of Bruntt et al. (2010); and a prior enforcing a main-sequence (MS) mass–radius relationship. This MS prior is based on that discussed in Collier Cameron et al. (2007), but is only applied to the stellar radius. The stellar mass is estimated using the calibration of Enoch et al. (2010).

To distinguish between models that use different combinations of priors, we minimize the reduced χ^2 for the spectroscopic data; in cases where there is little to choose between the different sets of input conditions, we gravitate towards the model with the fewest free parameters. In what follows, we refer to χ^2 as the combined χ^2 for the complete data set, $\chi^2_{\rm RV}$ as the value for the spectroscopic RV data only, and $\chi^2_{\rm red}$ as the reduced χ^2 for the spectroscopic data alone. Note also that we refer to the projected spin–orbit misalignment angle as λ, as is more common in the literature, not β as used by T10 (strictly $\lambda = -\beta$).

4 ROSSITER–Mc LAUGHLIN RESULTS

4.1 WASP-16

WASP-16b (Lister et al. 2009, hereafter L09) is a close Jupiter analogue orbiting a solar-type star with a period of 3.12 d. The planet is somewhat less massive than Jupiter but of comparable radius, whilst the host star is similar in mass, radius and metallicity to the Sun, but exhibits significant lithium depletion. Our updated spectroscopic analysis using the HARPS spectra yields a projected stellar rotation velocity of $v \sin I = 2.3 \pm 0.4\,\rm km\,s^{-1}$.

Our original estimate of stellar jitter produced fits with $\chi^2 \approx 1.6$, leading us to re-estimate the jitter following Wright (2005). We calculated line strengths for the calcium H and K emission lines in each of the HARPS spectra, and used these to estimate values for the chromospheric activity metric S. These were then calibrated against the Mount Wilson sample (see e.g. Baliunas et al. 1995), and absolute magnitudes of the stars were calculated using Gray (1992). We eventually adopted the 20th percentile value of $3.6\,\rm m\,s^{-1}$ as a conservative estimate of the jitter.

Removing the requirement for the system to obey an MS mass–radius relationship (equation 6 in Collier Cameron et al. 2007) produced changes of between 0 and 2 per cent in the stellar mass and radius, leading to increases in the stellar density of between 1 and 4 per cent, for no discernible improvement in fit (Table 2). Comparing impact parameter values, we find that we obtain an average value of $\bar{b} = 0.83^{+0.03}_{-0.04}$ for the cases both with and without the MS prior active. The parameter S (Collier Cameron et al. 2007),

$$S = -2 \ln P(M_*, R_*) = \frac{R_* - R_0}{\sigma_R^2}, \quad (1)$$

used to measure the discrepancy between the stellar radius from the $(J - H)$ colour and that returned by the MCMC algorithm, increases from an average of 0.17 to 0.34 when the prior is removed, a relatively small increase as suggested by the modest changes in stellar parameters. We therefore find little to distinguish between the cases with the MS requirement applied, and those with the stellar radius freely varying, and choose not to apply this prior in our final solution.

Adding a long-term, linear RV trend produced no improvement in $\chi^2_{\rm red}$, and with a magnitude of $|\dot{\gamma}| < 3\,\rm m\,s^{-1}\,yr^{-1}$ we disregard the possibility that there is a such a trend in the spectroscopic data. Adding a prior on the spectroscopic $v \sin I$ similarly gave almost no difference in the quality of the fit obtained. For most combinations of priors, our analysis returned $v \sin I \approx 1.2 \pm 0.3\,\rm km\,s^{-1}$, significantly slower than the spectroscopic value.

Allowing the eccentricity to float again led to no significant improvement in the fit, and all of the values of e returned by our various combinations of priors were consistent with $e = 0$ to within 2σ. We tested these small eccentricity values using equation (27) of Lucy & Sweeney (1971), which adopts a null hypothesis of a circular orbit and considers an orbit to be eccentric if this is rejected at the 5 per cent significance level. This F-test indicated that none of the eccentricities was significant, and thus that a circular orbit is favoured.

We therefore adopt as our conclusive solution the case without the MS prior active, with no prior on $v \sin I$, no long-term trend

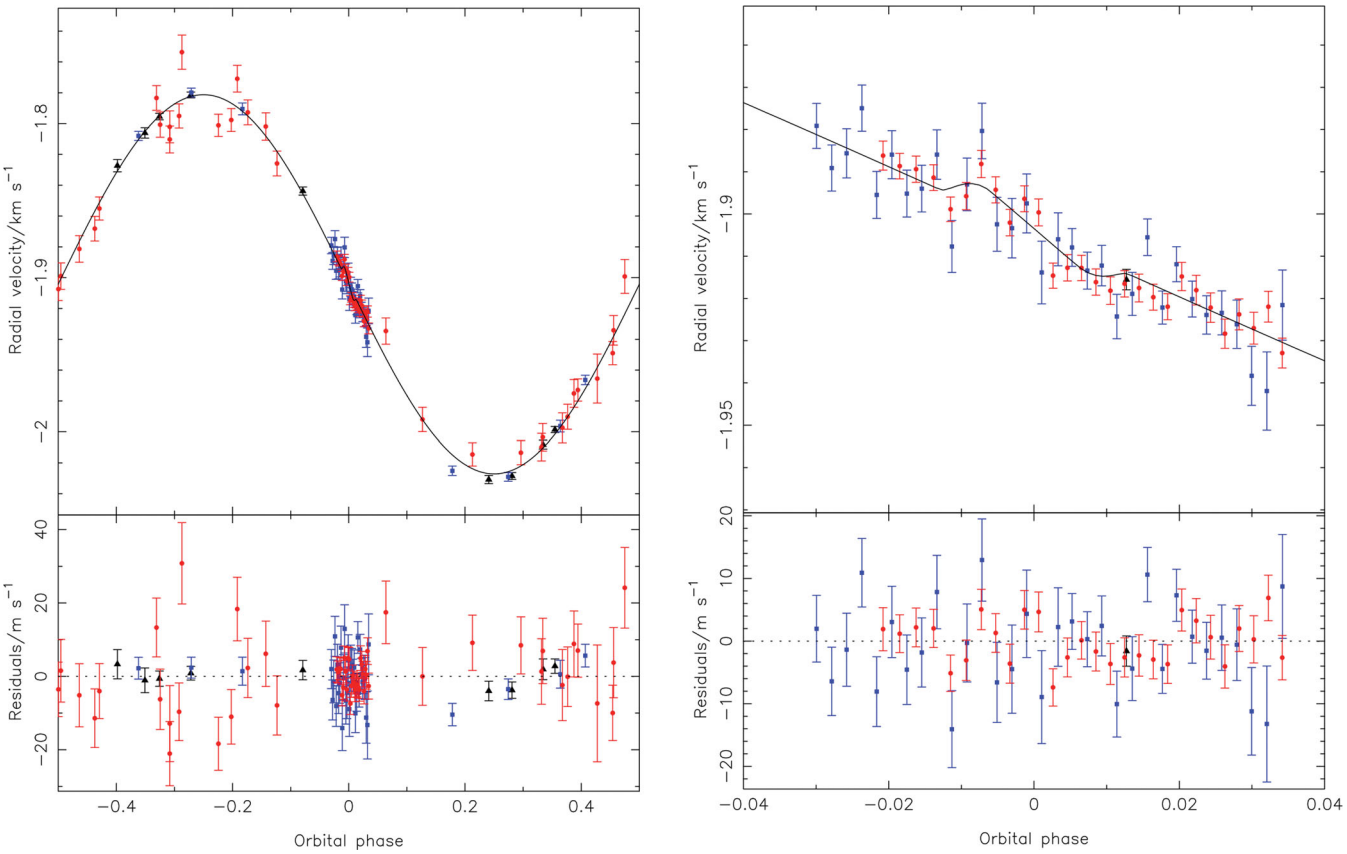

Figure 1. Results from the fit to the data for WASP-16 using $e = 0$, no long-term radial velocity trend, no prior on the spectroscopic $v \sin I$ and without forcing the mass–radius relationship. Black, filled triangles represent data from CORALIE. Blue, filled squares represent data from the first HARPS run. Red, filled circles represent data from the second HARPS run. The best-fitting model is plotted as a solid black line. Top left: complete radial velocity reflex motion curve. Bottom left: residuals from the RV fit, exhibiting no correlation with phase. Top right: close-up of the transit region from the radial velocity curve showing the RM effect, along with the residuals. Bottom right: residuals for the RV data within the RM window.

in velocity and a circular orbit, but we stress that changing the priors had little impact on the parameter values returned by the MCMC algorithm. Our adopted solution (Fig. 1) returns values of $\lambda = -4.^{\circ}2^{+11.0}_{-13.9}$ and $v \sin I = 1.2^{+0.4}_{-0.5}\,\mathrm{km\,s^{-1}}$; this is significantly slower than the spectroscopic value of $v \sin I$ that we obtained from spectral analysis. However, an alternative analysis of the HARPS spectra using the calibration of Gray (2008) provides an estimate of $v \sin I = 1.2 \pm 0.5$, in good agreement with the value that we found from our model. Our solution also indicates a high impact parameter of $0.82^{+0.01}_{-0.02}$ that reduces the likelihood of a degeneracy developing between λ and $v \sin I$. Examination of Fig. 2(b) highlights this, with a triangular distribution that is centred close to $\lambda = 0^{\circ}$. The main section of this distribution lies within the limits $|\lambda| < 20^{\circ}$, providing further evidence for the well-aligned system that was suggested by our best-fitting RM angle. From L09, we note that the host star has $T_{\rm eff} = 5700 \pm 150$ K, which places it in the 'cool' category of W10; an aligned orbit therefore fits their hypothesis quite nicely.

As previously noted, the amplitude of the RM anomaly for WASP-16 is quite small (see Fig. 1). The aligned nature of the system suggests that this can be put down to the star being an old, slowly rotating star, which would be consistent with the age estimate reported by L09, which suggests an age >5 Gyr based on a lack of detectable lithium. A second possible explanation could be that we are in fact viewing the host star almost pole-on, which could still be consistent with an orbit that is aligned in the plane of the sky. This would lead to a low projected rotation velocity, and a transit across the pole of the star would have a small RM amplitude, as observed here. The minimum stellar inclination is limited by the observed lithium depletion,[1] but such a structure would imply a younger age for the star owing to the rapid true stellar rotation. Interestingly, isochronal analysis in L09 implies an age of $2.3^{+5.8}_{-2.2}$ Gyr, lower than the limit implied by the lithium depletion. However, new isochronal fits, using our results and a range of stellar models, returned ages of $4.7^{+3.3}_{-4.3}$ Gyr (Padova models; Marigo et al. 2008), $4.8^{+1.2}_{-3.3}$ Gyr (Yonsei–Yale models; Demarque et al. 2004), $6.0^{+5.0}_{-4.0}$ Gyr (Teramo models; Pietrinferni et al. 2004) and $5.0^{+4.9}_{-3.8}$ Gyr Victoria-Regina Stellar Structure (VRSS) (models; VandenBerg, Bergbusch & Dowler 2006). These ages further support the case for a slowly rotating host star, and are consistent with the star's observed lithium abundance.

Careful analysis of the HARPS spectra allowed us to measure the chromospheric Ca II H&K emission. We find that $\log(R'_{\rm HK}) = -5.10 \pm 0.15$, indicating a low level of chromospheric activity. This rules out the possibility that the star is misaligned along the line of sight, as we would expect much greater calcium emission from a young, rapidly rotating star. We note that this agrees with the work of Schlaufman (2010), who finds no evidence for

[1] The abundance of lithium gives us a minimum age, as stated. If we assume that gyrochronology is applicable, then this provides a maximum true stellar rotation velocity. This in turn allows us to use the detected $v \sin I$ to calculate the minimum possible stellar inclination.

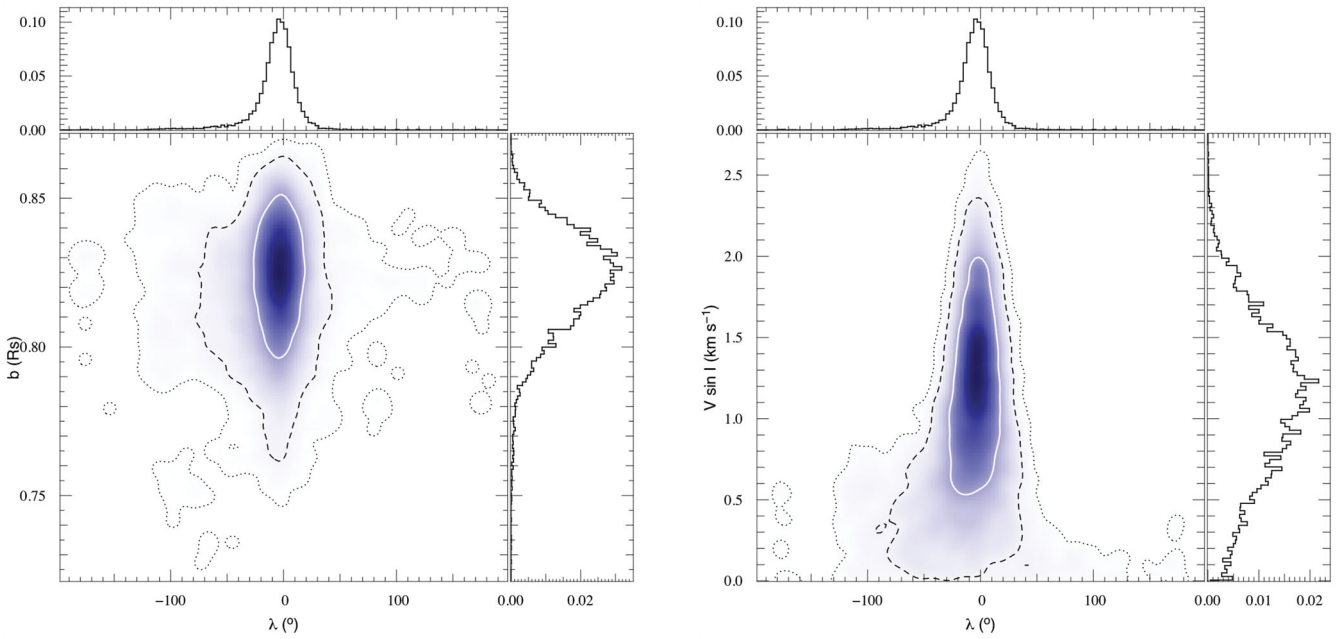

Figure 2. Posterior probability distributions derived from the Markov chains, for the fit to WASP-16 described in Fig. 1. The white contours mark the 62.87 per cent confidence regions, the black, dashed contours the 95.45 per cent confidence regions, and the black, dotted contours the 99.73 per cent confidence regions. Marginalized, 1D distributions are displayed in the side panels. Left: b and λ. Right: $v \sin I$ and λ. This distribution has a triangular shape, and $\lambda = 0$ falls within the central body of the distribution. Both distributions have poorly constrained 99.73 per cent confidence regions, and show a slight bias towards negative values of λ.

line-of-sight misalignment in the WASP-16 system. Following Watson et al. (2010), we calculate $P_{\rm rot} = 30.2^{+4.7}_{-3.8}$ d, which implies an age of $3.8^{+1.2}_{-0.8}$ Gyr for WASP-16 according to the gyrochronology method of Barnes (2007) using the updated coefficients of Meibom, Mathieu & Stassun (2009) and James et al. (2010). A recent reanalysis of the WASP-1 and WASP-2 systems (Albrecht et al. 2011) highlighted the fact that in systems with low-amplitude, low signal-to-noise ratio RM anomalies, the angles reported tend towards 0° and 180° owing to the greater probability density in the distribution for λ. The same study cautions readers against drawing strong conclusions of alignment in such cases. Our data for WASP-16 certainly show some of the characteristics discussed in the Albrecht et al. study, and we have indeed found a well-aligned system with λ close to 0.

However, there are other methods by which the alignment angle of a planetary orbit can be deduced. Doppler tomography is an established method for mapping velocity variations in binary stars (e.g. Albrecht et al. 2007, 2009), but its application to transiting exoplanets is in its infancy. The technique has, to date, been used to study HD 189733 (Collier Cameron et al. 2010b), WASP-33 (Collier Cameron et al. 2010a) and WASP-3 (Miller et al. 2010), and is best suited to analysing hot, rapidly rotating exoplanet host stars. WASP-16 A exhibits neither of these attributes, but analysis is ongoing (Miller et al., in preparation) and indications are that it gives similar results for the obliquity angle of this system. An independent detection of the RM effect, also suggesting alignment, was announced at IAU Symposium 276 by Winn, and we look forward to the published results with interest.

4.2 WASP-25

WASP-25b (Enoch et al. 2011, hereafter E11) is a significantly bloated, sub-Jupiter mass planet orbiting a solar-type, somewhat metal-poor host star with an orbital period of 3.76 d. A full set of results from our analysis is displayed in Table 3. One RV measurement was found to lie at 3σ from the best-fitting model, and to be consistent with the out of transit RV curve. This datum was omitted from our analysis, and will be discussed further later.

We found that allowing the eccentricity to float led to a negligible difference in $\chi^2_{\rm red}$, and that the eccentricity values being found were within 2σ of 0. We therefore concluded that the small eccentricity values being returned were arising owing to the biases inherent in the MCMC method (Ford 2006), and that the orbit of WASP-25 is circular. In this we agree with E11. We confirmed this conclusion regarding a circular orbit using the F-test of Lucy & Sweeney (1971), which returned very high probabilities of the small eccentricity values having arisen by chance.

We found little difference between the quality of fit for the equivalent cases with the MS mass–radius relation forced on the system and those without the same constraint. The relaxation of this prior leads to larger values of λ, but also increases the discrepancy between the stellar mass and radius values. The stellar mass value varies little between runs, but relaxing the MS prior reduces the stellar radius by between 2 and 3 per cent, dependent on the other priors being applied. This leads to an increase in the stellar density of between 7 and 12 per cent from $\bar{\rho}_{*,\,\rm MS} \approx 1.22\rho_\odot$ to $\bar{\rho}_{*,\,\rm no\,MS} \approx 1.34\rho_\odot$, averaged across all combinations of the other priors. Considering the impact parameter, we find that relaxing the MS requirement gives a value of $\bar{b} = 0.38^{+0.16}_{-0.22}$, whilst using the prior returns $\bar{b} = 0.44^{+0.11}_{-0.12}$, both averaged across all other combinations of priors. The S parameter increases from an average of 3.56 to 5.92 when the prior is removed. In light of these differences, we elect to apply the MS prior in our final analysis.

Adding a long-term linear trend in RV improved the $\chi^2_{\rm spec}$ of the solution, but the value of the trend varied significantly between runs, ranging from ≈2 to ≈105 m s^{-1} yr^{-1}. We also found that in

Table 3. A comparison of the χ^2 and $\chi^2_{\rm red}$ values for WASP-25 for each combination of Bayesian priors. All values of χ^2 include the Bayesian penalties applicable for that combination of priors.

$v \sin I$ prior	MS prior	$\dot{\gamma}$ (ms^{-1} yr^{-1})	Eccentricity	$v \sin I$ (km s^{-1})	λ (°)	χ^2	$\chi^2_{\rm RV}$	$\chi^2_{\rm red}$
Off	Off	0	$0.011^{+0.010}_{-0.008}$	2.8 ± 0.3	$17.9^{+9.8}_{-8.6}$	$142\,00 \pm 169$	104 ± 14	1.3 ± 0.2
Off	On	0	$0.013^{+0.013}_{-0.009}$	2.8 ± 0.3	$15.9^{+7.5}_{-7.3}$	$141\,95 \pm 168$	103 ± 14	1.3 ± 0.2
Off	Off	$103.8^{+25.5}_{-29.6}$	$0.013^{+0.014}_{-0.009}$	2.9 ± 0.3	$16.8^{+9.5}_{-9.4}$	$141\,84 \pm 168$	90 ± 13	1.1 ± 0.2
Off	On	$-10.3^{+13.6}_{-10.1}$	$0.011^{+0.013}_{-0.008}$	2.8 ± 0.3	$14.9^{+6.6}_{-7.1}$	$141\,97 \pm 169$	101 ± 14	1.3 ± 0.2
Off	Off	0	0	2.9 ± 0.3	14.6 ± 6.7	$142\,00 \pm 169$	104 ± 14	1.3 ± 0.2
Off	On	0	0	2.9 ± 0.3	$17.0^{+8.5}_{-8.1}$	$141\,99 \pm 169$	103 ± 14	1.3 ± 0.2
Off	Off	$96.1^{+28.7}_{-26.6}$	0	2.8 ± 0.3	$18.8^{+10.1}_{-8.6}$	$141\,89 \pm 168$	91 ± 13	1.1 ± 0.2
Off	On	$2.4^{+0.4}_{-0.3}$	0	2.8 ± 0.2	$12.7^{+8.4}_{-5.7}$	$137\,54 \pm 166$	103 ± 14	1.3 ± 0.2
2.6 ± 0.4	Off	0	$0.013^{+0.014}_{-0.009}$	2.8 ± 0.2	$15.6^{+8.9}_{-8.4}$	$141\,94 \pm 168$	103 ± 14	1.3 ± 0.2
2.6 ± 0.4	On	0	$0.011^{+0.011}_{-0.008}$	2.8 ± 0.2	$14.5^{+7.6}_{-6.7}$	$142\,00 \pm 169$	104 ± 14	1.3 ± 0.2
2.6 ± 0.4	Off	$100.4^{+28.6}_{-28.4}$	$0.013^{+0.014}_{-0.009}$	2.8 ± 0.2	$16.8^{+9.2}_{-9.0}$	$141\,83 \pm 168$	90 ± 13	1.1 ± 0.2
2.6 ± 0.4	On	$97.1^{+28.0}_{-25.8}$	$0.011^{+0.013}_{-0.008}$	2.8 ± 0.2	$15.3^{+7.5}_{-6.6}$	$141\,87 \pm 168$	91 ± 14	1.1 ± 0.2
2.6 ± 0.4	Off	0	0	2.8 ± 0.2	$16.8^{+9.7}_{-8.8}$	$141\,98 \pm 169$	104 ± 14	1.3 ± 0.2
2.6 ± 0.4	On	0	0	2.8 ± 0.2	$14.8^{+6.6}_{-6.9}$	$142\,02 \pm 169$	104 ± 14	1.3 ± 0.2
2.6 ± 0.4	Off	$104.8^{+21.9}_{-35.6}$	0	2.8 ± 0.2	$17.1^{+9.1}_{-7.9}$	$141\,85 \pm 168$	91 ± 13	1.1 ± 0.2
2.6 ± 0.4	On	95.4 ± 26.5	0	2.8 ± 0.2	$14.5^{+6.7}_{-7.2}$	$141\,89 \pm 168$	91 ± 13	1.1 ± 0.2

some cases the models produced when a trend was applied showed a notable offset from the RV data in transit. To check whether a trend was truly present in the system, two additional RV measurements were obtained using HARPS on 2010 August 25 and 26. Analysing these in conjunction with previously obtained data shows no evidence for a long-term RV trend, and so we disregard this possibility for our final solution. Introducing a prior on the spectroscopic $v \sin I$ produced no improvement to the quality of fit to the data, irrespective of the other flags. We do not therefore apply such a prior in our final solution, and take this opportunity to obtain a separate measurement of the projected stellar rotation speed.

Taking the results of these investigations into account, we select the solution with $e = 0$, no long-term linear trend in RV and no prior on $v \sin I$, with the MS mass–radius relation enforced (see Fig. 3). This gives $\lambda = 14\overset{\circ}{.}6 \pm 6\overset{\circ}{.}7$, a detection of the RM effect at 2.2σ from 0. We also obtain a value for the stellar rotation of $v \sin I = 2.9 \pm 0.3$ km s^{-1}, slightly greater than but in agreement with our updated spectroscopic value of 2.6 ± 0.4 km s^{-1}. The impact parameter for this solution is 0.44 ± 0.04. No correlation is apparent between $v \sin I$ and λ, although there is evidence for a correlation between the impact parameter and λ (see Fig. 4). It is possible that this correlation is responsible for the poor fit of the model to some parts of the RM data.

The mechanism responsible for the outlier that we omitted from our analysis is unknown, although we note that Simpson et al. (2010) experienced a similar situation in their analysis of the WASP-38 system, positing seeing changes of telescope guiding faults as possible causes. We suggest a third mechanism; the discrepant point might be caused by the planet traversing a stellar spot. In such a situation, the spot would mask the presence of the planet, causing the RV measurement to diverge from the standard RM anomaly pattern. This scenario was suggested to explain a similar anomaly in the data for the WASP-3 system (Tripathi et al. 2010), but we note that the divergence from the RM effect in that case showed a gradual rise and fall rather than the delta function change observed here, and was eventually attributed to the effect of moonlight. Unfortunately, we lack simultaneous photometry from the night of the observed spectroscopic transit, which would show the presence of such a spot. It is also possible that some form of transient event, such as a white light stellar flare, is responsible for the drastic, sudden change in measured RV for this point, although. Such events were discussed in the context of LQ Hya (Montes et al. 1999), and were observed to produce chromospheric disturbance in the core of otherwise normal spectral lines. This dilution of the spectral lines could affect the continuum level during the flare event, and potentially lead to anomalous redshifting for a short period of time. Such an event would have to be very short duration, however, and coincide with the planet's path across the stellar disc.

Should we consider WASP-25 to be aligned? W10 put forward a criterion of $\lambda \geq 10^\circ$ to $>3\sigma$ for misalignment; our result for WASP-25 clearly fails this test. T10 suggest an alternative criterion of $\lambda > 30^\circ$ as the limit above which we can be sure a system is misaligned given the average magnitude of the errors in λ that are found by analysis of the RM effect. WASP-25 also misses this target by some margin. But the data for the RM effect appear to be slightly asymmetric in Fig. 3(b), suggesting that the system is misaligned (although we note that the best-fitting model does not reflect this).

This slight asymmetry in the RM anomaly might arise as a result of some form of systematic effect. We have already mentioned the possibility of stellar spots in the context of the anomalous datum omitted from our analysis. Could they also provide a possible explanation for the asymmetry? Consider a star on which stellar spots are more numerous in one hemisphere than the other during the planetary transit, but on which they lie away from the transit chord. As the planet transits the more spotty hemisphere, it will hide a comparatively larger fraction of the photosphere and therefore mask a greater contribution to the overall flux than when it is transiting the less spotty hemisphere. The half of the anomaly corresponding to the spotted hemisphere would therefore have a greater amplitude than the half of the anomaly corresponding to the unspotted hemisphere, leading to an asymmetric RM effect. If the difference in the number and/or size of spots between the two hemispheres is small, then the asymmetry would be only minor. This interesting systematic was discussed by Albrecht et al. (2011)

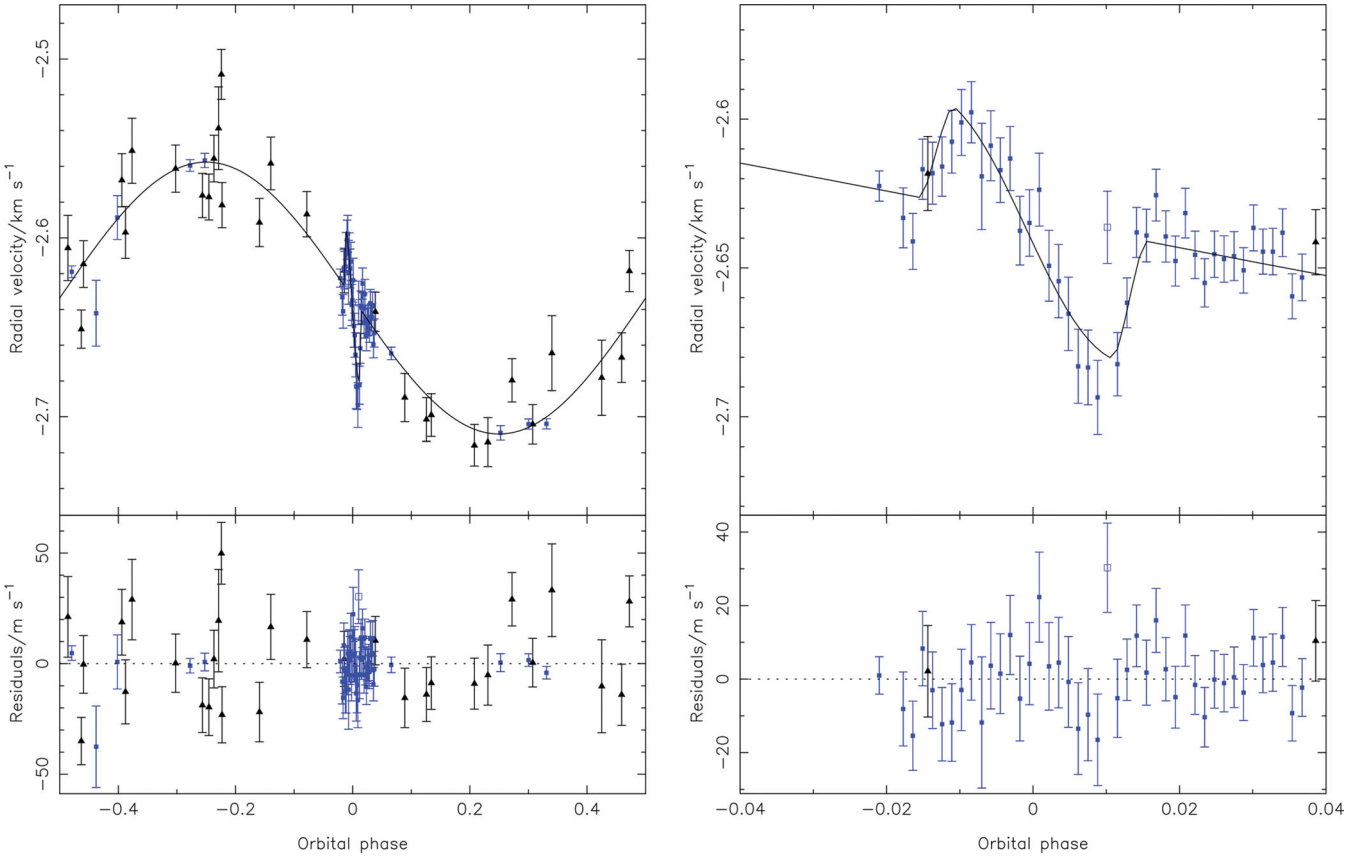

Figure 3. Results from the fit to the data for WASP-25 of our optimal solution: a circular orbit, no long-term RV trend and no prior on the spectroscopic $v \sin I$. The MS mass–radius relation was not enforced. The point denoted by the open square was found to lie 3σ from the best-fitting model, and was not included in the analysis. Legend as for Fig. 1.

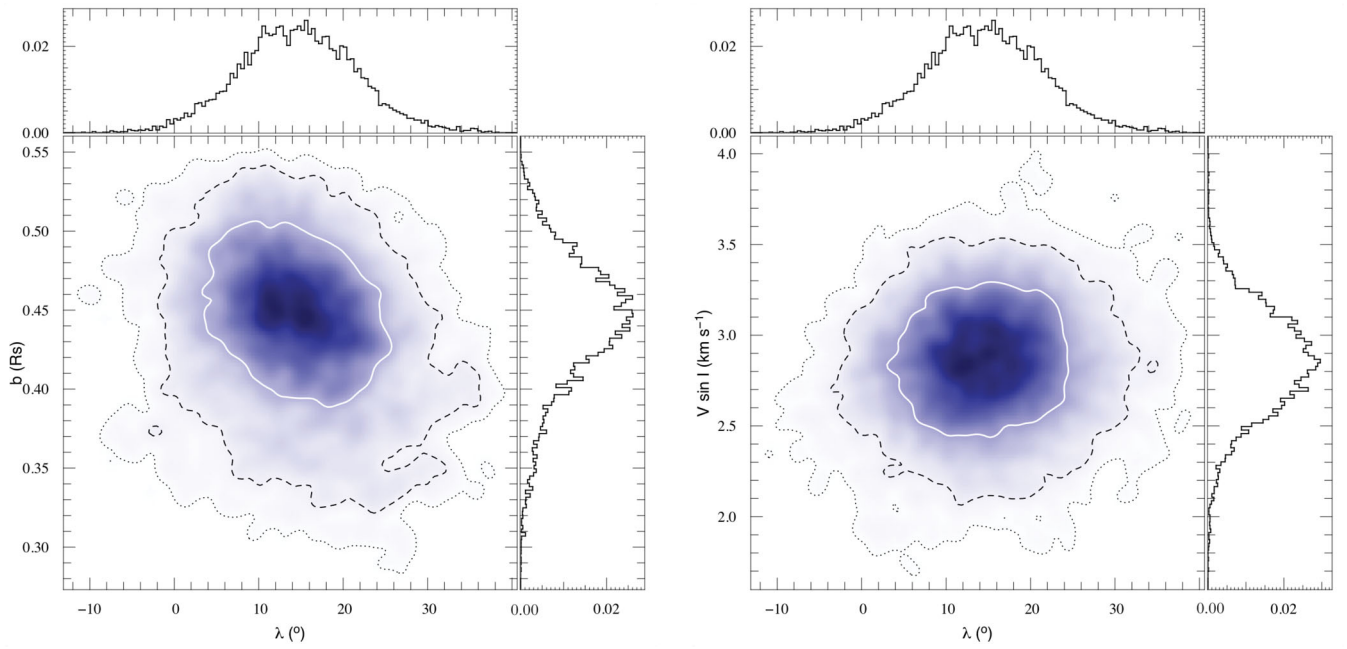

Figure 4. Posterior probability distributions, derived from the Markov chain, for the fit to the data for WASP-25 described in Fig. 3. Key as for Fig. 2. Left: b and λ. There appears to be some small level of correlation between the two parameters. Right: $v \sin I$ and λ. $\lambda = 0$ falls outside the 68.27 per cent confidence contour, but within the 95.45 per cent confidence contour, indicating a moderately significant detection of λ.

for the case of WASP-2, and also seems to have played a role in the analysis of the CoRoT-2 RM in Bouchy et al. (2008). In the case of WASP-25, the approaching, blueshifted hemisphere would be required to have a slightly greater density of stellar spots than the receding, redshifted hemisphere, which would also lead back to the possibility of a transient event being responsible for the anomalous datum.

We will return to the question of WASP-25's alignment in Section 6.

4.3 WASP-31

WASP-31 (Anderson et al. 2011b) is a bloated, $0.5\,M_{\rm Jup}$ planet orbiting an F-type star of subsolar metallicity with a period of 3.5 d. The host star is a moderately rapid rotator, with $v \sin I = 8.1 \pm 0.5$ from spectroscopy. Full results of our analysis can be found in Table 4.

We found no difference between the $\chi^2_{\rm red}$ values for any combination of priors. We found that imposing the MS mass–radius relation had little effect on the fit to the spectroscopic data, but had a deleterious effect on the stellar parameters. Removing the prior produced an increase in stellar radius of between 3 and 6 per cent and a decrease in the stellar mass of between 1 and 2 per cent, leading to a decrease in stellar density of between 8 and 15 per cent from $\bar{\rho}_{*,\,\rm MS} \approx 0.67\rho_\odot$ to $\bar{\rho}_{*,\,\rm no\,MS} \approx 0.62\rho_\odot$, averaged across all other combinations of priors. Comparing the impact parameter and S statistic, we find $\bar{b} = 0.79^{+0.03}_{-0.05}$ and $\bar{S} = 10.2$ with no MS prior applied, and $\bar{b} = 0.77^{+0.03}_{-0.04}$ with $\bar{S} = 2.9$ when the requirement for the star to be on the MS is enforced. Owing to the much more favourable S statistic, and the influence on the stellar parameters, we elect to use results which account for the MS relationship. Adding a linear velocity trend gave no discernible difference in the quality of the fit to the spectroscopic data, and with a magnitude of $|\dot{\gamma}| < 13\,{\rm m\,s^{-1}\,yr^{-1}}$ we conclude that no such trend is present in the system. Adding a prior on the spectroscopic $v \sin I$ made little difference to the results despite the relatively rapid rotation, so we again choose the simpler route and neglect such a prior. Finally, we choose a circular solution; the F-test of Lucy & Sweeney (1971) shows that the small eccentricity values returned when e is allowed to float are insignificant.

Our optimal solution is therefore that obtained with no $v \sin I$ prior, no velocity trend, the MS prior active and $e = 0$. This set of priors gives $\lambda = 2\overset{\circ}{.}8 \pm 3\overset{\circ}{.}1$, leading to the conclusion that the WASP-31 system is well aligned (see Figs 5 and 6). It is worth noting that this would be the conclusion whichever combination of priors we chose, as all of the values of λ that we obtained lie within 1.2σ of 0°. The impact parameter is $0.77^{+0.01}_{-0.02}$. The stellar rotation for this solution has a value of $v \sin I = 7.5 \pm 0.7\,{\rm km\,s^{-1}}$. As with our result for WASP-16, this is slower than the spectroscopic value, but in this case the value agrees to within 1σ. Again, an alternative analysis using the calibration of Gray (1992) returns a value of $v \sin I$ ($7.5 \pm 0.5\,{\rm km\,s^{-1}}$) more similar to our MCMC result. WASP-31 is not included in the sample of Schlaufman (2010) owing to its time of publication. In order to check the possibility of misalignment along the line of sight, we follow the method of Schlaufman and calculate the rotation statistic, Θ. The age of WASP-31 A is somewhat uncertain, however; its lithium abundance, gyrochronology and the presence of a close companion all suggest ages of $\approx$1 Gyr, whilst previous stellar model fits imply an older age of 4 ± 1 Gyr. We reassess the isochronal fit for the system, obtaining ages of $4.0^{+1.8}_{-1.0}$ Gyr (Padova models), $2.8^{+1.4}_{-1.0}$ Gyr (Yonsei–Yale models), $3.5^{+2.3}_{-1.3}$ Gyr (Teramo models) and $2.8^{+1.6}_{-1.2}$ Gyr (VRSS models). Using these estimates, we calculate values of $\Theta = -4.5$, -3.0, -3.7 and -2.8, respectively; WASP-31 is therefore rotating more rapidly than expected given its age in both cases. The chance of significant misalignment along the line of sight therefore seems slim; the inclination of the WASP-31 b's orbit is $84\overset{\circ}{.}6 \pm 0\overset{\circ}{.}2$, leaving little room for an increase in rotation velocity owing to line-of-sight misalignment.

5 INTEGRATION INTO THE ENSEMBLE OF RESULTS

The analysis of W10 provides a good starting point for integrating our new results into the existing ensemble of RM

Table 4. A comparison of the χ^2 and $\chi^2_{\rm red}$ values for WASP-31 for each combination of Bayesian priors. All values of χ^2 include the Bayesian penalties applicable for that combination of priors.

$v \sin I$ prior	MS prior	$\dot{\gamma}$ (${\rm ms^{-1}yr^{-1}}$)	Eccentricity	$v \sin I$ (${\rm km\,s^{-1}}$)	λ ($^\circ$)	χ^2	$\chi^2_{\rm RV}$	$\chi^2_{\rm red}$
Off	Off	0	$0.027^{+0.032}_{-0.019}$	7.5 ± 0.8	$2.8^{+1.1}_{-2.9}$	14703 ± 171	64 ± 11	0.9 ± 0.2
Off	On	0	$0.031^{+0.029}_{-0.019}$	$7.7^{+0.9}_{-0.8}$	$3.6^{+2.9}_{-3.5}$	14708 ± 172	64 ± 11	0.9 ± 0.2
Off	Off	$6.1^{+8.1}_{-8.4}$	$0.023^{+0.031}_{-0.017}$	7.4 ± 0.7	$2.8^{+2.9}_{-2.8}$	14700 ± 171	63 ± 11	0.9 ± 0.2
Off	On	$12.6^{+8.4}_{-7.6}$	$0.037^{+0.035}_{-0.016}$	7.8 ± 0.8	$3.1^{+3.0}_{-2.8}$	14695 ± 171	63 ± 11	0.9 ± 0.2
Off	Off	0	0	7.5 ± 0.7	2.7 ± 3.0	14702 ± 171	64 ± 11	0.9 ± 0.2
Off	On	0	0	7.5 ± 0.7	2.8 ± 3.1	14706 ± 172	64 ± 11	0.9 ± 0.2
Off	Off	$6.4^{+7.9}_{-8.1}$	0	7.5 ± 0.7	$2.4^{+2.9}_{-2.7}$	14698 ± 171	63 ± 11	0.9 ± 0.2
Off	On	$5.3^{+8.8}_{-7.7}$	0	$7.3^{+0.7}_{-0.6}$	$3.0^{+3.4}_{-3.1}$	14698 ± 171	64 ± 11	0.9 ± 0.2
8.1 ± 0.5	Off	0	$0.023^{+0.029}_{-0.017}$	7.9 ± 0.4	$2.5^{+2.8}_{-2.6}$	14693 ± 171	64 ± 11	0.9 ± 0.2
8.1 ± 0.5	On	0	$0.041^{+0.033}_{-0.027}$	8.0 ± 0.5	$3.2^{+3.0}_{-2.9}$	14703 ± 171	64 ± 11	0.9 ± 0.2
8.1 ± 0.5	Off	$-0.1^{+9.2}_{-6.6}$	$0.022^{+0.033}_{-0.016}$	$7.9^{+0.4}_{-0.5}$	$2.7^{+2.9}_{-2.7}$	14698 ± 171	63 ± 11	0.9 ± 0.2
8.1 ± 0.5	On	$3.4^{+5.7}_{-4.6}$	$0.038^{+0.023}_{-0.018}$	8.0 ± 0.4	3.0 ± 2.7	14702 ± 171	64 ± 11	0.9 ± 0.2
8.1 ± 0.5	Off	0	0	7.9 ± 0.4	$2.8^{+2.7}_{-2.9}$	14697 ± 171	64 ± 11	0.9 ± 0.2
8.1 ± 0.5	On	0	0	7.8 ± 0.4	$3.0^{+3.0}_{-2.9}$	14701 ± 171	65 ± 11	0.9 ± 0.2
8.1 ± 0.5	Off	$6.1^{+10.3}_{-8.6}$	0	7.8 ± 0.4	$2.7^{+2.7}_{-2.9}$	14701 ± 171	64 ± 11	0.9 ± 0.2
8.1 ± 0.5	On	$5.4^{+7.7}_{-8.5}$	0	7.9 ± 0.4	$3.0^{+3.0}_{-2.9}$	14705 ± 171	65 ± 11	0.9 ± 0.2

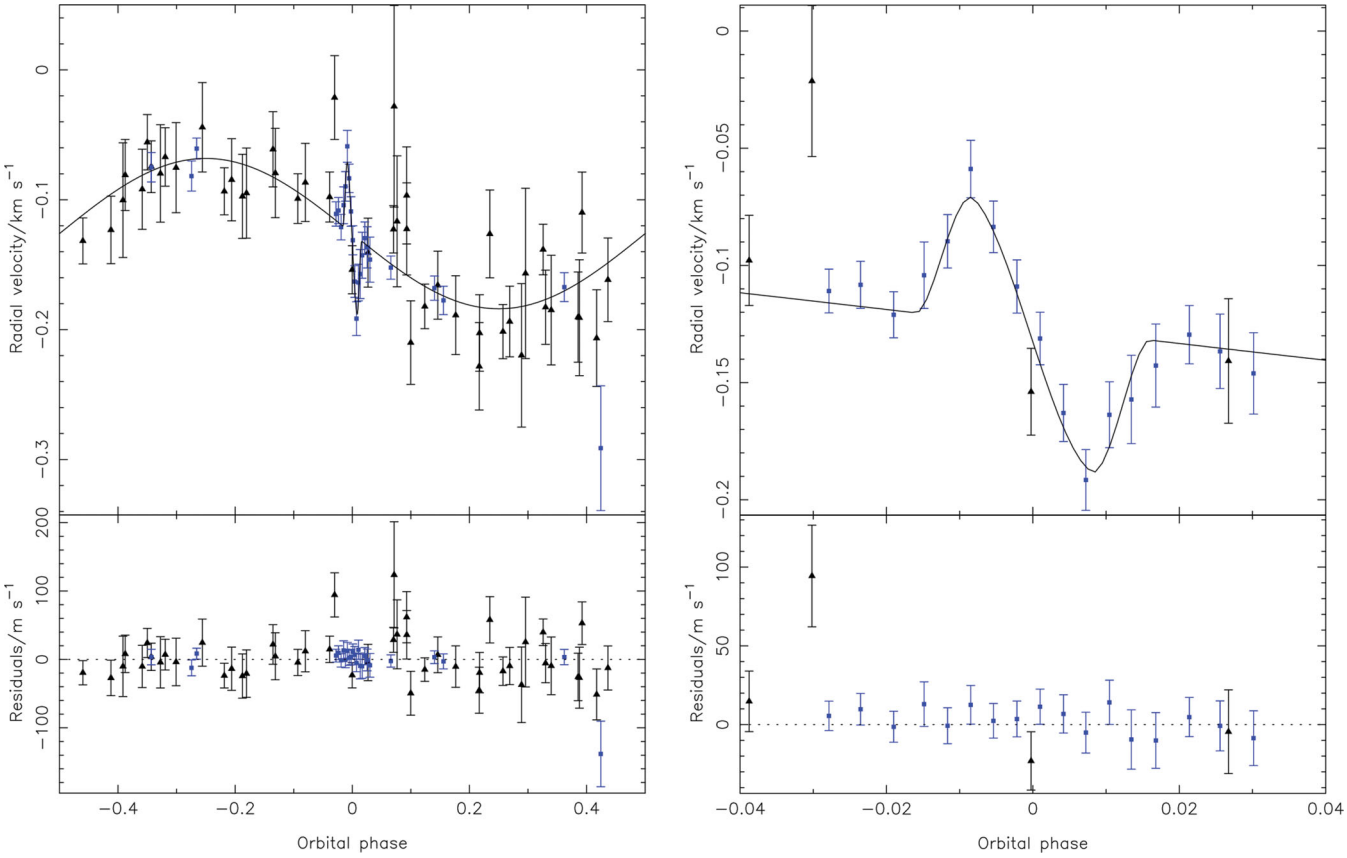

Figure 5. Results from the fit to the data for our adopted solution for WASP-31, with a circular orbit, no prior on the spectroscopic $v \sin I$, no long-term radial velocity trend and the mass–radius relationship applied. Legend as for Fig. 1.

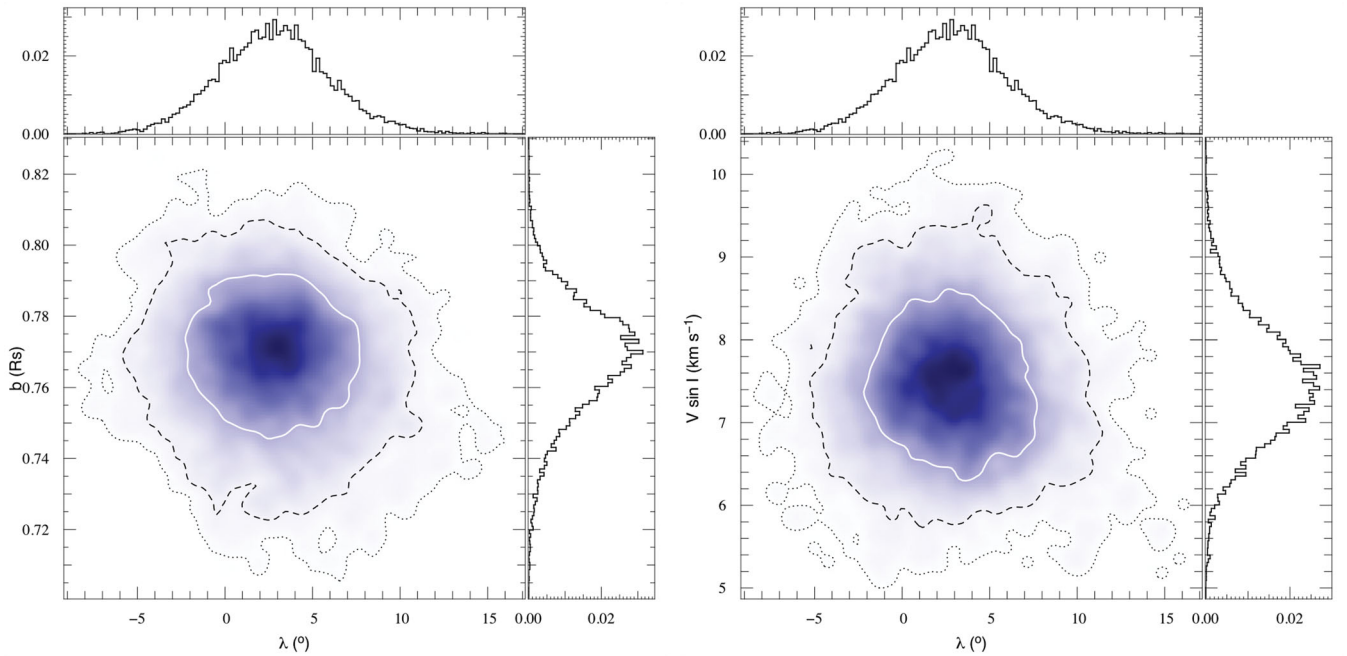

Figure 6. Posterior probability distributions, derived from the Markov chain, for the fit to the data for WASP-31 described in Fig. 5. Key as for Fig. 2. Left: b and λ. Right: $v \sin I$ and λ. $\lambda = 0$ lies well within the main body of the distribution.

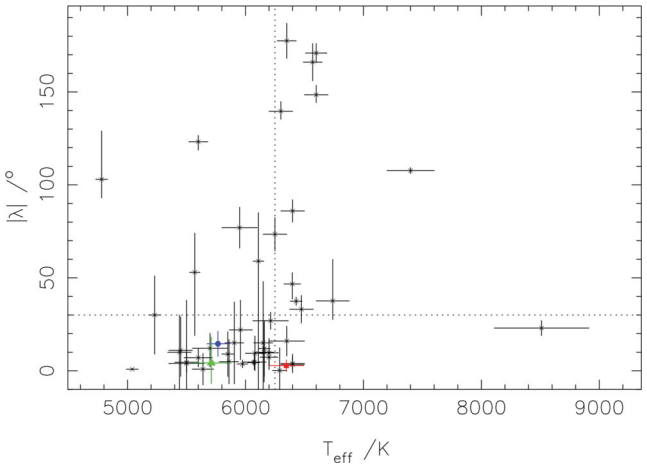

Figure 7. Projected stellar obliquity, λ, as a function of stellar effective temperature for all systems with confirmed measurements. WASP-16 is marked by a green, filled triangle, WASP-25 by a blue, filled circle, and WASP-31 by a red, filled square. The vertical dotted line marks the distinction between 'cool' and 'hot' systems, whilst the horizontal dotted line marks 30°, the angle above which a system is considered to be misaligned in W10 and T10.

measurements. Fig. 7 reproduces Fig. 2 from their paper, with the addition of all complete RM measurements made since its publication [except WASP-23 (Triaud et al. 2011), for which the result is still highly uncertain, and WASP-26 (Anderson et al. 2011a), which showed only a very low amplitude and was classed as a non-detection]; we list these planets in Table 5. We also elect to include most of the systems that W10 disregard during their analysis as having insufficiently precise measurements of λ [2] in order to provide a full picture of the current state of RM analysis. Whilst it is true that making a definitive statement regarding alignment is more difficult for these systems owing to their large uncertainties, the criteria for granting misaligned status should take account of this. We are also interested in comparing our new measurements to the general form of the current ensemble. Omitting the systems listed above does not simplify this task, so we elect to include them.

WASP-31 has an effective temperature of 6300 ± 100 K, which falls within 1σ of the border between the 'hot' and 'cool' categories of W10, albeit tending towards the 'hot' side. We cannot therefore draw any conclusions as to how it affects the trend proposed in that paper.

With an effective temperature of 5750 ± 100 K, WASP-25 falls into the 'cool' category ($T_{\rm eff} \leq 6250$ K) of W10, which they find to be preferentially aligned – their sample gives a probability of misalignment for 'cool' stars of 0.17. Updating this result using our expanded sample changes the probability either to 0.20 using the criterion of W10, or to 0.13 using the criterion of $|\lambda| > 30^\circ$ from T10. It is worth noting here that the apparently large differences in misalignment probability between the two criteria are an artefact of the sample size, which is still relatively small at 48 systems (30 'cool', 18 'hot'). Switching between the two criteria only changes the number of aligned systems by two for the 'cool' subsample, and has no effect on the number of misaligned systems in the 'hot' subsample. Under both criteria, the apparent alignment of WASP-25 b's orbit is in accordance with the W10 hypothesis.

[2] HAT-P-2, CoRoT-1, CoRoT-3, HD 149026, Kepler-8, TrES-1 and TrES-2. See references within W10. Although WASP-2 has a measured value for λ, the most recent analysis of the system failed to detect a signal (Albrecht et al. 2011) and thus we continue to exclude this system.

WASP-16, $T_{\rm eff} = 5700 \pm 150$ K, is also classified as a 'cool' system. All available information points towards this system being well aligned, and it therefore fits well with the hypothesis of W10.

The final interesting point about Fig. 7 is the apparent lack of systems with mildly retrograde, close to polar orbits. There are currently only two systems with $80^\circ \leq \lambda \leq 110^\circ$, and only one more with $110^\circ \leq \lambda \leq 140^\circ$. This relatively unpopulated region is less notable when considering ψ owing to the increased size of the error bars, but it is still apparent. We speculate that truly polar orbits are perhaps unstable for some reason. Or perhaps it is simply our inability to determine the inclination of the stellar rotation axis that is at fault. It may be that some 'aligned' systems actually have close to polar orbits if this angle is accounted for. It may also be that we simply have yet to observe very many systems in this region of the parameter space, and future publications may provide the data to fill this underpopulated area.

It has not been remarked upon before in this context, but a drop in the number of systems at mid-range obliquity angles is clearly predicted by the theoretical ψ angular distribution of Fabrycky & Tremaine (2007). It also clearly shows up in the angular distribution for the complete set of known obliquity angles (fig. 10 in T10). We reproduce this figure in Fig. 8, adding the probability distributions of the planets in Table 5 as well as those of the planetary systems from this study. ψ, the true misalignment angle, is given by

$$\cos\psi = \cos I \cos i + \sin I \sin i \cos\lambda, \quad (2)$$

where I is the inclination of the stellar rotation axis to the line of sight, and i is the inclination of the orbital axis to the line of sight. To calculate the ψ distribution for each planet, we carried out 10^6 Monte Carlo simulations, drawing values for I from a uniform cos I distribution to represent the case in which stellar rotation axes are randomly oriented on the sky. We also accounted for the error bars on i and λ by drawing values from a Gaussian distribution with our optimal solution values as the mean values, and scaled to the uncertainties in those values. The individual planets' distributions were then summed to produce our total distribution, which is similar to that of T10, and still compares favourably to the theoretical histogram from Fabrycky & Tremaine (2007). The drop in probability at mid-range angles is in line with the underpopulated region of Fig. 7, and our additions bring the primary, low-angle peak closer in shape to the theoretical distribution. The overall shape of the secondary peak is less clear; it is still dominated by contributions from individual systems owing to the smaller number of planets with strongly misaligned orbits as compared to the number of aligned or weakly misaligned systems, but appears as though it may be broader and more shallow than the theoretical prediction.

Fig. 8 requires the assumption that the I, the stellar inclination, is isotropic and that the angular distribution is unimodal. However, the discussion of W10 implies that the distribution is in fact bimodal. A clearer demonstration of the agreement between theoretical predictions and current observations is therefore to look at the distribution in λ. This requires the converse transformation of the predicted ψ distribution of Fabrycky & Tremaine (2007) into λ.

We reproduce the lower panel of fig. 9 from T10, taking into account the additional measurements of λ from Table 5. For HAT-P-7 and HAT-P-14, both of which have published $\lambda > 180^\circ$, we used the negative angle equivalent $(360 - \lambda)$. This cumulative λ distribution avoids both of the assumptions inherent in Fig. 8. Agreement between the observational data and the theoretical predictions of Fabrycky & Tremaine (2007) has been improved, particularly for low- to mid-range angles, but the observational data are still slightly lacking in high-obliquity systems compared to the theoretical

Table 5. Relevant data for the planetary systems for which the Rossiter–McLaughlin effect has been characterized since the publication of W10. We add these systems to the W10 sample to bring the ensemble of results up to date and allow us to better analyse the place of WASP-25 and WASP-31 within that ensemble.

System	i (°)	$v \sin I$ (km s^{-1})	$T_{\rm eff}$ (K)	λ (°)	Reference
CoRoT-18	$86.5^{+1.4}_{-0.9}$	8.0 ± 1.0	5440 ± 100	10 ± 20	Hébrard et al. (2011a)
HAT-P-4	$88.76^{+0.89}_{-1.38}$	5.83 ± 0.35	5860 ± 80	4.9 ± 11.9	Winn et al. (2011)
HAT-P-6	85.51 ± 0.35	7.5 ± 1.6	6570 ± 80	166 ± 10	Hébrard et al. (2011b)
HAT-P-8	87.5 ± 1.4	14.5 ± 0.8	6200 ± 80	$-17^{+9.2}_{-11.5}$	Latham et al. (2009); Moutou et al. (2011)
HAT-P-9	86.5 ± 0.2	12.5 ± 1.8	6350 ± 150	-16 ± 8	Shporer et al. (2009); Moutou et al. (2011)
HAT-P-11	$89.17^{+0.46}_{-0.60}$	$1.00^{+0.95}_{-0.56}$	4780 ± 50	103^{+26}_{-10}	Winn et al. (2010a)
HAT-P-14	83.52 ± 0.22	8.18 ± 0.49	6600 ± 90	189.1 ± 5.1	Winn et al. (2011)
HAT-P-16	86.6 ± 0.7	3.9 ± 0.8	6158 ± 80	-10.0 ± 16	Buchhave et al. (2010); Moutou et al. (2011)
HAT-P-23	85.1 ± 1.5	7.8 ± 1.6	5905 ± 80	15 ± 22	Bakos et al. (2011); Moutou et al. (2011)
HAT-P-30	83.6 ± 0.4	3.07 ± 0.24	6304 ± 88	73.5 ± 9.0	Johnson et al. (2011)
KOI-13.01	85.0 ± 0.4	65 ± 10	8511 ± 400	23 ± 4	Barnes, Linscott & Shporer (2011)
WASP-1	90 ± 2	$0.7^{+1.4}_{-0.5}$	6110 ± 45	-59^{+99}_{-26}	Albrecht et al. (2011)
WASP-7	$87.2^{+0.9}_{-1.2}$	14 ± 2	6400 ± 100	86 ± 6	Southworth et al. (2011); Albrecht et al. (2012)
WASP-19	$79,4 \pm 0.4$	4.63 ± 0.26	5500 ± 100	4.6 ± 5.2	Hellier et al. (2011)
WASP-22	88.26 ± 0.91	4.42 ± 0.34	5958 ± 98	22 ± 16	Anderson et al. (2011a)
WASP-24	83.64 ± 0.29	7.0 ± 0.9	6075 ± 100	-4.7 ± 4.0	Simpson et al. (2010)
WASP-38	$88.83^{+0.51}_{-0.55}$	8.58 ± 0.39	6150 ± 80	15^{+33}_{-43}	Simpson et al. (2010)
XO-3	82.5 ± 1.5	18.4 ± 0.2	6430 ± 50	37.4 ± 2.2	Winn et al. (2009b); Hirano et al. (2011b)
XO-4	88.8 ± 0.6	8.9 ± 0.5	6397 ± 70	-46.7 ± 7.1	Narita et al. (2010)

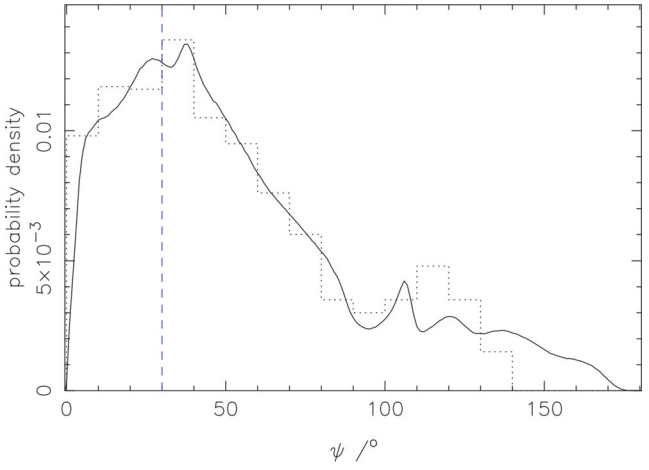

Figure 8. The total distribution of the true obliquity angle, ψ, for the complete sample of systems for which λ has been measured. The dotted histogram represents the theoretical distribution of Fabrycky & Tremaine (2007). The dashed line represents the limit of $\psi = 30°$ above which a system is considered to be misaligned. The overall forms are comparable, and the total ψ distribution is similar to fig. 10 of T10. The shape of the primary peak agrees well with theoretical predictions. The overall shape of the secondary, high-angle peak in the distribution is less clear, but may be more shallow and broader than anticipated. The sudden drop in probability density at mid-range angles, around $\psi \approx 90°$, has become more pronounced when compared to the distribution of T10.

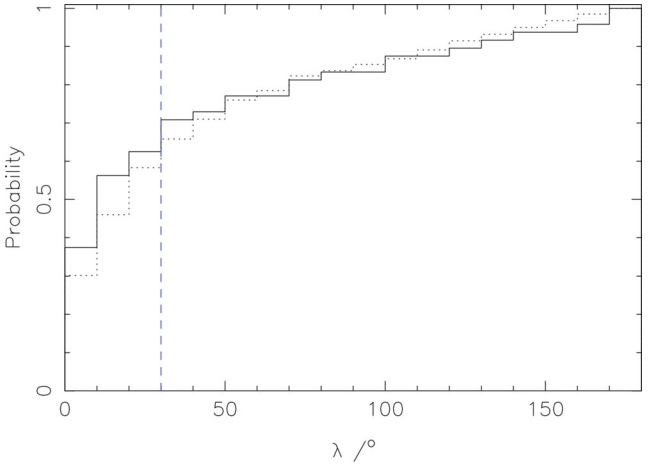

Figure 9. Cumulative probability histogram for λ. The solid line denotes observational data, whilst the dotted line denotes the theoretical distribution of Fabrycky & Tremaine (2007), converted from ψ to λ. The vertical blue, dashed line marks $\lambda = 30°$, the limit above which a planetary orbit is considered to be misaligned. The agreement between the two distributions has improved with the addition of measurements made since the publication of T10, particularly at mid-range angle, prograde orbits, but the observational data are still lacking in high-obliquity systems compared to the theoretical prediction.

histogram, whilst showing more low-obliquity systems than expected (Fig. 9).

6 A NEW MISALIGNMENT TEST

The RM effect has now been measured for 48 transiting exoplanets, but as of yet there seems little consensus as to the best way of classifying them as aligned or misaligned. For most of the systems with measurements of λ, this is not a serious problem; either $|\lambda| > 90°$, or the error bars are such that the obliquity is consistent with zero. But as the number of RM measurements continues to grow, there will be an increasing number of systems in a similar situation to WASP-25, which exhibits a mildly asymmetrical RM anomaly but does not fulfil any of the current misalignment criteria.

There are two main criteria currently in use by the community. W10 use $|\lambda| > 0°$ at $\geq 3\sigma$ significance to define a misaligned system. T10 take $|\lambda| > 30°$ as their threshold, on the basis that errors in the obliquity angle are of the order of 10°, and therefore this gives 3σ significance as well. We would like to introduce a new test for misalignment that takes a completely different approach to these.

We consider the set of WASP planets for which the RM effect has been characterized using RV data, including the systems presented in this study. We neglect the WASP-33 system for which the misalignment angle has been measured only through Doppler tomography (Collier Cameron et al. 2010a), and disregard the ambiguous results for WASP-23 (Triaud et al. 2011) and WASP-2 (Albrecht et al. 2011). For reasons of consistency, we use the RV-based solution of Tripathi et al. (2010) for our initial conditions for WASP-3, rather than the more recent tomographical study of Miller et al. (2010). The full set of planets sample is listed in Table 6.

Our test is based on the Bayesian information criterion (BIC Liddle 2007):

$$\mathrm{BIC} = \chi^2_{\mathrm{RV}} + k\ln(n), \tag{3}$$

where k is the number of parameters and n is the number of data. Changing the value of λ only affects the form of the model RV curve in-transit; we therefore just consider those RV points that lie within a region of the RV curve around phase 0 defined by the fractional transit width when computing the second term of the BIC. The number of parameters changes according to the choice of priors applied to the MCMC run; adding a long-term RV trend, fitting the RM effect and allowing the eccentricity to float all add one or more additional parameters to the model.

We carry out two MCMC analyses for each of the systems in our sample, using the same combination of priors for both. The first analysis allows both $\sqrt{v\sin I}\cos\lambda$ and $\sqrt{v\sin I}\sin\lambda$ to float, whilst the second forces an aligned orbit by fixing $\sqrt{v\sin I}\sin\lambda = 0$. We calculate the BIC for both runs, before calculating $B = \mathrm{BIC}_{\mathrm{align}}/\mathrm{BIC}$. For the three systems presented herein, we use our adopted solutions, and carry out an additional run to provide the aligned case. We plot the results for all of the systems as a function of the sky-projected alignment angle.

We find several distinct groups of systems within our results, which lead us to define three categories of alignment into which systems with RM measurements can be classified. Five systems, including WASP-16 and WASP-31, were found to have $B \leq 0.980$, implying that the model with $\lambda = 0^\circ$ provides a better fit that the free-floating λ model. Of these five systems, all would be classified as aligned according to either of the existing misalignment criteria. A further four systems, including WASP-25, are clustered around $B = 1.00$, forming a distinct group in Fig. 10(b). Forcing an aligned orbit would seem to make little difference to the quality of the fit between data and model in these cases. Of these systems, three would clearly be classed as aligned according to W10 and T10, but the fourth (WASP-1) would actually be classed as misaligned according to W10. The remaining systems clearly lie distinct from those discussed so far, and many are clearly classifiable as misaligned, with $|\lambda| > 100^\circ$ and $B > 1.5$.

In light of these results, we define three categories of alignment. Systems for which $B \leq 0.99$ we classify as misaligned. Those with $B \geq 1.01$ we classify as aligned. Systems falling between these categories, with $0.99 < B < 1.01$, we classify as of indeterminate alignment. We would also define a fourth category, that of 'no detection', as containing those systems with $v\sin I$ consistent with 0 to within 1σ, but our current sample contains no systems that meet this requirement.

Some of the systems in Table 6 warrant a little more examination. WASP-16, despite the relatively poor quality of the RM data that we obtained, can be more strongly considered aligned than WASP-31 with its high-quality data. This is an interesting, if puzzling, result, but does provide further evidence to support our previous conclusion of an aligned system for WASP-16. WASP-25 is classified as undetermined under our new criteria, possibly owing to the relatively poor match between the shape of the RM anomaly and the best-fitting model. However, we note that it lies very close to the boundary between the 'undetermined' and 'misaligned' categories. Our new MCMC runs for WASP-1 and WASP-4 produce very large error bars on λ, but end up in different categories despite both

Table 6. Relevant data for our new misalignment criterion, for a sample of WASP planets with existing Rossiter–McLaughlin measurements. λ values are those obtained from our new MCMC analyses. BIC values were calculated from the spectroscopic χ^2 values, using the number of in-transit RV measurements only. Our new misalignment criterion defines systems with a BIC ratio $B \geq 1.01$ as misaligned, those with $B \leq 0.99$ as aligned, and those with $0.99 < B < 1.01$ as of indeterminate status.

System	Reference	λ ($^\circ$)	$v\sin I$ (km s^{-1})	BIC	$\mathrm{BIC}_{\mathrm{align}}$	ΔBIC	B
WASP-1	Albrecht et al. (2011)	$60.2^{+23.3}_{-126.6}$	1.3 ± 0.5	255.2 ± 22.6	256.7 ± 22.7	1.5	1.006
WASP-3	Tripathi et al. (2010)	$37.9^{+9.3}_{-11.8}$	$12.9^{+1.1}_{-0.8}$	294.7 ± 24.3	308.0 ± 24.8	13.3	1.045
WASP-4	T10	$42.0^{+14.3}_{-75.6}$	$2.5^{+0.4}_{-0.3}$	86.8 ± 13.2	91.3 ± 13.5	4.5	1.052
WASP-5	T10	$26.2^{+8.1}_{-6.8}$	3.5 ± 0.2	186.0 ± 19.3	199.2 ± 20.0	12.1	1.071
WASP-6	Gillon et al. (2009)	$-7.5^{+20.9}_{-19.1}$	$1.7^{+0.3}_{-0.2}$	134.7 ± 16.4	132.0 ± 16.2	-2.7	0.980
WASP-7	Albrecht et al. (2012)	$85.0^{+9.4}_{-8.0}$	$26.3^{+1.3}_{-1.2}$	285.8 ± 23.9	451.7 ± 30.1	165.9	1.580
WASP-8	Queloz et al. (2010)	$-106.7^{+3.0}_{-3.5}$	$2.8^{+0.4}_{-0.3}$	380.3 ± 27.8	1092.5 ± 46.7	712.2	2.873
WASP-14	Joshi et al. (2009)	$-28.0^{+5.0}_{-5.5}$	2.8 ± 0.3	171.2 ± 18.5	193.5 ± 19.7	22.3	1.130
WASP-15	T10	$-133.8^{+11.7}_{-9.5}$	$4.5^{+0.4}_{-0.3}$	154.4 ± 17.6	555.7 ± 33.3	401.3	3.599
WASP-17	T10	$-134.5^{+5.3}_{-7.1}$	9.8 ± 0.3	342.7 ± 26.2	986.9 ± 44.4	644.2	2.880
WASP-18	T10	$20.5^{+10.5}_{-11.5}$	12.9 ± 0.3	118.8 ± 15.4	119.0 ± 15.4	0.2	1.002
WASP-19	Hellier et al. (2011)	$-1.6^{+5.6}_{-5.4}$	3.2 ± 0.2	81.5 ± 12.8	79.8 ± 12.6	-1.7	0.979
WASP-24	Simpson et al. (2010)	$-6.9^{+5.4}_{-5.8}$	$5.1^{+0.4}_{-0.3}$	123.1 ± 15.7	119.8 ± 15.5	-3.3	0.973
WASP-38	Simpson et al. (2010)	$-6.1^{+3.3}_{-38.7}$	8.2 ± 0.3	241.3 ± 22.0	240.8 ± 21.9	-0.5	0.998
WASP-16	This study	$-4.2^{+11.0}_{-13.9}$	$1.2^{+0.4}_{-0.5}$	115.6 ± 15.2	112.1 ± 15.0	-3.5	0.970
WASP-25	This study	14.6 ± 6.7	2.9 ± 0.3	116.5 ± 15.3	117.5 ± 15.3	0.8	1.009
WASP-31	This study	2.8 ± 3.1	7.5 ± 0.7	73.7 ± 12.1	72.2 ± 12.0	-1.5	0.980

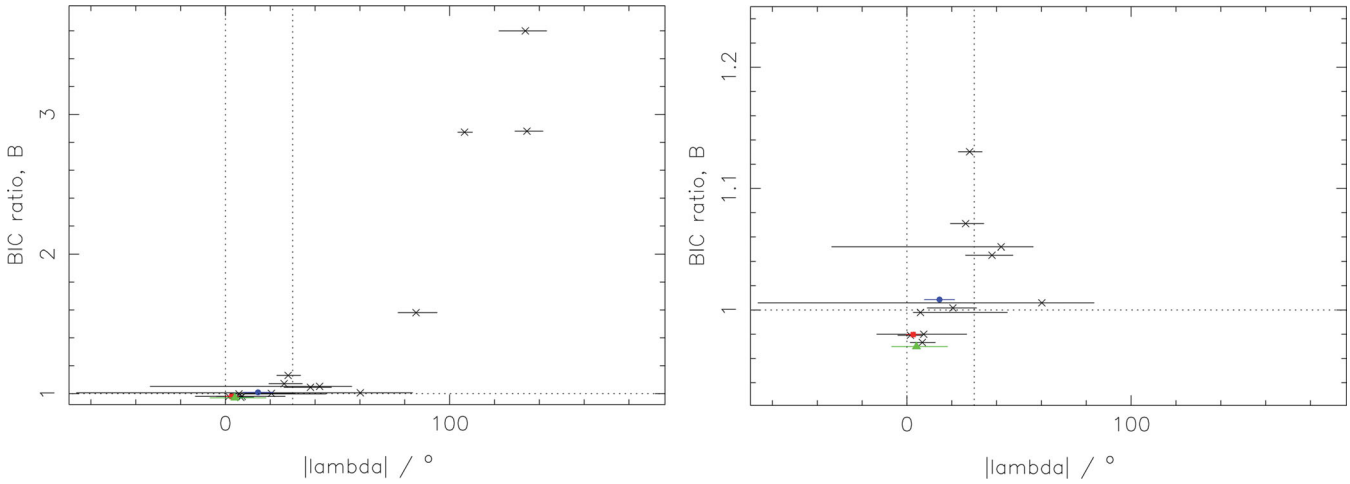

Figure 10. B as a function of λ for the sample of planets in Table 6, as well as the systems presented in this study. WASP-16 is denoted by a filled, green triangle. WASP-25 is denoted by a filled, blue circle. WASP-31 is denoted by a filled, red square. The horizontal dotted line marks $B = 1.00$. The two vertical dotted lines denote $|\lambda| = 0^\circ$ and 30°, the existing criterion for misalignment. Left: all data. Right: a close-up of the heavily populated region in the lower left of the plot, around $B = 1.00$ and $|\lambda| = 0^\circ$. This shows the separation of the systems into several distinct groupings, which lead us to define three categories of alignment. This changes the existing classification of some systems.

failing the T10 criterion of misalignment. Examining their respective RM anomalies, we note that both have very low amplitudes, but that the data for WASP-4 are of significantly better quality than that for WASP-1. It is likely that this is responsible for the difference in classification. In addition, T10 noted a substantial correlation between λ and $v \sin I$ for WASP-4, arising due to the low impact parameter, which may be producing the large lower error. WASP-38 also exhibits a significant error bar on λ, and we again note that the RM data are again of somewhat poor quality. New observations of WASP-38 using HARPS may help in improving the quality of the results for the system, allowing us to draw firmer conclusions (Brown et al, in preparation).

7 CONCLUSIONS

We have presented analysis of the RM effect for WASP-16, WASP-25 and WASP-31. We find WASP-16 to have a very low amplitude signal, but the use of two complete spectroscopic transits has enabled us to determine a sky-projected alignment angle of $\lambda = -4\overset{\circ}{.}2^{+11.0}_{-13.9}$. For WASP-25, we find a mildly asymmetric RM anomaly with $\lambda = 14\overset{\circ}{.}6 \pm 6\overset{\circ}{.}7$, and for WASP-31 we obtain $\lambda = 2\overset{\circ}{.}8 \pm 3\overset{\circ}{.}1$, indicating a well-aligned system.

Since WASP-31 lies so close to the effective temperature that divides the classes of 'hot' and 'cool' planet hosts, we cannot say how its alignment affects the pattern proposed by W10. WASP-25, on the other hand, at first appears to strengthen their hypothesis, with the existing misalignment criteria of both W10 and T10 labelling it aligned. We have also presented a new method for determining the alignment or otherwise of an exoplanetary orbit. Our test is based on the BIC statistic, and bases the misalignment or alignment of a system on the ratio of the values of the BIC for the free λ case and the aligned case. We classify systems with $B \geq 1.01$ as misaligned, those with $B \leq 0.99$ as aligned, and those with $0.99 \leq B \leq 1.01$ as of indeterminate classification. WASP-25 falls in this last category, albeit very close to the boundary with the 'misaligned' classification.

The results presented herein bring the analysis of the ensemble of systems with confirmed stellar obliquities up to date. Our results have done little to change the overall picture presented by T10, instead strengthening the agreement with theoretical predictions for the distributions of both the projected and true stellar obliquities. We should not be too hasty to assume that we have solved the problem of hot Jupiter migration, however; new discoveries are constantly causing us to re-evaluate our current understanding.

ACKNOWLEDGMENTS

The authors would like to thank the referee, Josh Winn, for his insightful comments and constructive suggestions. DJAB would also like to thank Teryuki Hirano for assistance with improving the RM modelling, and Simon Albrecht for helpful discussions regarding analysis of these systems. MG is FNRS Research Associate. IB would like to thank the Fundação para a Ciência e a Tecnologia (FCT), Portugal, through the form of grant reference PTDC/CTE-AST/098528/2008. The WASP Consortium consists of representatives from the Universities of Keele, Leicester, The Open University, Queens University Belfast and St Andrews, along with the Isaac Newton Group (La Palma) and the Instituto de Astrofisca de Canarias (Tenerife). The SuperWASP and WASP-S cameras were constructed and operated with funds made available from Consortium Universities and PPARC/STFC. This research has made use of NASA's Astrophysics Data System Bibliographic Services, and the ArXiv preprint service hosted by Cornell University.

REFERENCES

Albrecht S., Reffert S., Snellen I., Quirrenbach A., Mitchell D. S., 2007, A&A, 474, 565
Albrecht S., Reffert S., Snellen I. A. G., Winn J. N., 2009, Nat, 461, 373
Albrecht S. et al., 2011, ApJ, 738, 50
Albrecht S., Winn J. N., Butler R. P., Crane J. D., Shectman S. A., Thompson I. B., Hirano T., Wittenmyer R. A., 2012, ApJ, 744, 189
Anderson D. R. et al., 2011a, A&A, 534, A16
Anderson D. R. et al., 2011b, A&A, 531, A60
Bakos G. Á. et al., 2011, ApJ, 742, 116
Baliunas S. L. et al., 1995, ApJ, 438, 269
Barnes S. A., 2007, ApJ, 669, 1167
Barnes J. W., Linscott E., Shporer A., 2011, ApJ, 197, 10
Bouchy F. et al., 2008, A&A, 482, L25

Bruntt H. et al., 2010, MNRAS, 405, 1907
Buchhave L. A. et al., 2010, ApJ, 720, 1118
Claret A., 2000, A&A, 363, 1081
Collier Cameron A. et al., 2007, MNRAS, 380, 1230
Collier Cameron A. et al., 2010a, MNRAS, 407, 507
Collier Cameron A., Bruce V. A., Miller G. R. M., Triaud A. H. M. J., Queloz D., 2010b, MNRAS, 403, 151
Demarque P., Woo J.-H., Kim Y.-C., Yi S. K., 2004, ApJS, 155, 667
Enoch B., Collier Cameron A., Parley N. R., Hebb L., 2010, A&A, 516, A33
Enoch B. et al., 2011, MNRAS, 410, 1631 (E11)
Fabrycky D., Tremaine S., 2007, ApJ, 669, 1298
Fabrycky D. C., Winn J. N., 2009, ApJ, 696, 1230
Ford E., 2006, ApJ, 642, 505
Gillon M. et al., 2009, A&A, 501, 785
Gray D. F., 1992, PASP, 106, 1248
Gray D. F., 2008, The Observation and Analysis of Stellar Photospheres. Cambridge Univ. Press, Cambridge, UK
Hébrard G. et al., 2011a, A&A, 533, A130
Hébrard G. et al., 2011b, A&A, 527, L11
Hellier C., Anderson D. R., Collier-Cameron A., Miller G. R. M., Queloz D., Smalley B., Southworth J., Triaud A. H. M. J., 2011, ApJ, 730, L31
Hirano T., Suto Y., Winn J. N., Taruya A., Narita N., Albrecht S., Sato B., 2011a, ApJ, 742, 69
Hirano T., Narita N., Sato B., Winn J. N., Aoki W., Tamura M., Taruya A., Sato Y., 2011b, PASJ, 63, L57
James D. J. et al., 2010, A&A, 515, A100
Johnson J. A., Winn J. N., Albrecht S., Howard A. W., Marcy G. W., Gazak J. Z., 2009, PASP, 121, 1104
Johnson J. A. et al., 2011, ApJ, 735, 24
Joshi Y. C. et al., 2009, MNRAS, 392, 1532
Knutson H. A., Charbonneau D., Allen L. E., Burrows A., Megeath S. T., 2008, ApJ, 673, 526
Kozai Y., 1962, AJ, 67, 591
Latham D. et al., 2009, ApJ, 704, 1107
Liddle A. R., 2007, MNRAS, 377, L74
Lidov M. L., 1962, Planet. Space Sci., 9, 719
Lin D. N. C., Bodenheimer P., Richardson D. C., 1996, Nat, 380, 606
Lister T. A. et al., 2009, ApJ, 703, 752 (L09)
Lucy L. B., Sweeney M. A., 1971, AJ, 76, 544
McLaughlin D. B., 1924, ApJ, 60, 22
Marigo P., Girardi L., Bressan A., Groenewegen M. A. T., Silva L., Granato G. L., 2008, A&A, 482, 883
Mayor M. et al., 2003, The Messenger, 114, 20
Meibom S., Mathieu R. D., Stassun K. G., 2009, ApJ, 695, 679
Montes D., Saar S. H., Collier Cameron A., Unruh Y. C., 1999, MNRAS, 305, 45
Moutou C. et al., 2011, A&A, 533, A113
Narita N., Sato B., Hirano T., Tamura M., 2009, PASJ, 61, L35
Narita N., Hirano T., Sanchis-Ojeda R., Winn J. N., Holman M. J., Sato B., Aoki W., Tamura M., 2010, PASJ, 62, L61
Pietrinferni A., Cassisi S., Salaris M., Castelli F., 2004, ApJ, 612, 168
Pollacco D. et al., 2006, PASP, 118, 1407
Queloz D., Eggenberger A., Mayor M., Perrier C., Beuzit J. L., Naef D., Sivan J. P., Udry S., 2000a, A&A, 359, L13
Queloz D., Mayor M., Naef D., Santos N., Udry S., Burnet M., Confino B., 2000b, in Bergeron J., Renzini A., eds, The VLT Opening Symp., From Extrasolar Planets to Cosmology. Springer-Verlag, Berlin, p. 548
Queloz D. et al., 2010, A&A, 517, L1
Rossiter R. A., 1924, ApJ, 60, 15
Schlaufman K. C., 2010, ApJ, 719, 602
Shporer A. et al., 2009, ApJ, 690, 1393
Simpson E. K. et al., 2011, MNRAS, 414, 3023
Southworth J. et al., 2011, A&A, 527, A8
Tegmark M. et al., 2004, Phys. Rev. D, 69, 103501
Triaud A. et al., 2010, A&A, 524, A25 (T10)
Triaud A. et al., 2011, A&A, 531, A24
Tripathi A. et al., 2010, ApJ, 715, 421
VandenBerg D. A., Bergbusch P. A., Dowler P. D., 2006, ApJS, 162, 375
Watson C. A., Littlefair S. P., Collier Cameron A., Dhillon V. S., Simpson E. K., 2010, MNRAS, 408, 1606
Winn J. N., Johnson J. A., Albrecht S., Howard A. W., Marcy G. W., Crossfield I. J., Holman M. J., 2009a, ApJ, 703, L99
Winn J. N. et al., 2009b, ApJ, 700, 302
Winn J. N. et al., 2010a, ApJ, 723, L223
Winn J. N., Fabrycky D., Albrecht S., Johnson J. A., 2010b, ApJ, 718, L145 (W10)
Winn J. N. et al., 2011, AJ, 141, 63
Wright J. T., 2005, PASP, 117, 657

APPENDIX A: ADDITIONAL RESULTS

Table A1. Parameters from the best-fitting, adopted models for the three WASP planetary systems studied in the main text.

System	$v \sin I$ prior	MS prior	$\dot{\gamma}$ ($\mathrm{ms^{-1}\,yr^{-1}}$)	Eccentricity	Jitter ($\mathrm{m\,s^{-1}}$)	$v \sin I$ ($\mathrm{km\,s^{-1}}$)	λ (°)
WASP-16	Off	Off	0	0	1.0	$1.2^{+0.4}_{-0.5}$	$-4.2^{+11.0}_{-13.9}$
WASP-25	Off	On	0	0	3.6	2.9 ± 0.3	14.6 ± 6.7
WASP-31	Off	On	0	0	1.0	7.5 ± 0.7	2.8 ± 3.1

APPENDIX B: JOURNAL OF OBSERVATIONS

Table B1. Radial velocity data for WASP-16 obtained using the CORALIE high-precision echelle spectrograph.

HJD (−245 0000)	$T_{\rm exp}$ (s)	RV (km s^{-1})	$\sigma_{\rm RV}$ (km s^{-1})
4535.864 842	900	−1.997 72	0.015 91
4537.849 158	1427	−1.966 88	0.008 53
4538.858 364	1800	−2.007 34	0.008 99
4558.780 835	1800	−1.833 36	0.007 23
4560.709 473	1800	−2.005 13	0.007 25
4561.688 137	1800	−1.827 30	0.007 85
4589.705 102	1800	−1.842 55	0.008 75
4591.706 755	1800	−2.035 71	0.008 92
4652.495 906	1800	−1.824 93	0.008 08
4656.551 645	1800	−2.024 21	0.007 87
4657.577 293	1800	−1.966 40	0.009 57
4663.539 741	1800	−2.029 61	0.009 69
4664.616 769	1800	−1.785 90	0.011 08
4682.521 501	1800	−1.981 18	0.007 54
4881.869 213	1800	−2.022 45	0.008 13
4882.801 025	1800	−1.832 89	0.008 23
4884.737 094	1800	−2.045 65	0.007 78
4891.805 707	1800	−1.900 43	0.007 98
4892.723 980	1800	−1.834 13	0.008 91
4941.728 231	1800	−1.887 37	0.007 48
4943.730 102	1800	−2.046 77	0.007 53
4944.739 293	1800	−1.913 59	0.008 60
4945.799 895	1800	−1.858 15	0.008 07
4947.745 317	1800	−1.939 60	0.007 41
4948.673 112	1800	−1.829 92	0.007 43
4972.707 323	1800	−1.931 23	0.008 54
4975.733 486	1800	−1.931 44	0.011 00
4982.647 535	1800	−1.834 33	0.010 36
4984.642 389	1800	−2.042 10	0.008 92
4985.694 776	1800	−1.815 61	0.008 02
5391.544 362	1800	−1.803 13	0.008 67

Table B2. Radial velocity data for WASP-16, for the first transit obtained using the HARPS high-precision echelle spectrograph on the night of 2010 March 21.

HJD (−245 0000)	$T_{\rm exp}$ (s)	RV (km s^{-1})	$\sigma_{\rm RV}$ (km s^{-1})
5275.661 171	1800	−1.806 10	0.003 37
5275.907 691	1800	−1.781 44	0.001 88
5276.661 941	500	−1.882 64	0.005 33
5276.668 446	500	−1.892 63	0.005 46
5276.674 824	500	−1.889 14	0.005 83
5276.681 375	500	−1.878 45	0.005 47
5276.687 753	500	−1.899 00	0.005 57
5276.694 258	500	−1.889 47	0.005 69
5276.700 693	500	−1.898 68	0.005 55
5276.707 094	500	−1.897 50	0.005 52
5276.713 599	500	−1.889 45	0.005 86
5276.720 046	500	−1.911 21	0.006 14
5276.726 493	500	−1.896 50	0.006 23
5276.732 929	500	−1.883 85	0.006 57
5276.739 376	500	−1.905 96	0.006 40
5276.745 812	500	−1.906 86	0.007 04
5276.752 143	500	−1.901 01	0.006 98
5276.758 579	500	−1.917 36	0.007 42
5276.765 605	500	−1.909 50	0.006 27
5276.771 589	500	−1.911 43	0.004 47
5276.778 140	500	−1.916 92	0.004 39

Table B2 – *continued*

HJD (−245 0000)	$T_{\rm exp}$ (s)	RV (km s^{-1})	$\sigma_{\rm RV}$ (km s^{-1})
5276.784 344	500	−1.915 73	0.004 79
5276.790 838	500	−1.927 79	0.005 26
5276.797 459	500	−1.922 43	0.005 10
5276.803 964	500	−1.909 02	0.004 33
5276.810 411	500	−1.925 67	0.003 91
5276.816 441	500	−1.915 40	0.004 16
5276.823 178	500	−1.923 66	0.004 24
5276.829 336	500	−1.927 42	0.004 54
5276.835 887	500	−1.926 93	0.005 22
5276.842 334	500	−1.929 62	0.005 72
5276.848 723	500	−1.941 83	0.006 99
5276.855 228	500	−1.945 43	0.009 26
5276.861 907	500	−1.925 08	0.008 30
5277.630 948	1800	−2.028 47	0.002 22
5277.861 599	1800	−1.998 54	0.001 96
5278.632 376	1800	−1.827 33	0.003 98
5278.857 922	1800	−1.795 46	0.002 08
5279.627 285	1800	−1.843 79	0.002 64
5279.913 540	1500	−1.915 54	0.002 42
5280.624 797	1800	−2.030 79	0.002 66
5280.916 481	1200	−2.008 24	0.002 83

Table B3. Radial velocity data for WASP-16, for the second transit obtained using the HARPS high-precision echelle spectrograph on the night of 2011 May 12.

HJD (−245 0000)	$T_{\rm exp}$ (s)	RV (km s^{-1})	$\sigma_{\rm RV}$ (km s^{-1})
5685.845 943	900	−2.027 24	0.003 05
5687.838 150	900	−1.792 59	0.003 83
5692.662 149	900	−1.998 41	0.003 80
5692.796 210	900	−1.968 47	0.003 09
5693.517 817	900	−1.810 13	0.002 98
5693.800 775	900	−1.781 96	0.002 85
5694.581 176	600	−1.883 49	0.003 44
5694.588 340	600	−1.885 97	0.003 02
5694.595 389	600	−1.886 70	0.003 10
5694.602 900	600	−1.888 71	0.003 05
5694.610 180	600	−1.896 19	0.002 90
5694.616 904	500	−1.893 08	0.003 23
5694.623 386	500	−1.885 47	0.003 23
5694.629 531	500	−1.891 59	0.003 09
5694.635 631	500	−1.899 35	0.003 12
5694.641 904	500	−1.893 71	0.003 07
5694.648 003	500	−1.896 94	0.003 18
5694.654 149	500	−1.911 91	0.002 98
5694.660 364	500	−1.910 05	0.003 11
5694.666 406	500	−1.910 09	0.003 00
5694.672 609	500	−1.913 43	0.003 11
5694.678 824	500	−1.915 47	0.003 27
5694.684 924	500	−1.913 84	0.003 13
5694.691 070	500	−1.914 84	0.003 30
5694.697 227	500	−1.917 01	0.003 08
5694.703 373	500	−1.919 26	0.003 08
5694.709 460	500	−1.912 11	0.003 35
5694.715 664	500	−1.915 34	0.003 53
5694.721 821	500	−1.919 48	0.003 49
5694.727 979	500	−1.925 66	0.003 46
5694.734 078	500	−1.921 09	0.003 67
5694.740 351	500	−1.924 35	0.003 77
5694.746 612	500	−1.919 26	0.003 64
5694.752 596	500	−1.930 24	0.003 54
5695.501 446	900	−2.031 20	0.002 81

Table B4. Radial velocity data for WASP-25 obtained using the CORALIE high-precision echelle spectrograph.

HJD (−245 0000)	t_{exp} (s)	RV (km s^{-1})	σ_{RV} (km s^{-1})
4829.822 664	1800	−2.577 17	0.012 82
4896.769 798	1800	−2.651 05	0.010 69
4940.709 168	1800	−2.715 89	0.011 54
4941.704 336	1800	−2.618 55	0.011 53
4942.725 717	1800	−2.576 32	0.012 38
4943.637 434	1800	−2.618 28	0.012 46
4944.715 466	1800	−2.679 66	0.012 07
4945.726 530	1800	−2.614 67	0.013 05
4946.616 622	1800	−2.581 69	0.012 66
4947.601 618	1800	−2.641 33	0.010 96
4947.791 245	1800	−2.689 27	0.013 47
4948.613 002	1800	−2.704 18	0.010 98
4949.803 142	560	−2.551 32	0.018 19
4950.622 083	1800	−2.591 41	0.013 48
4951.695 324	1800	−2.701 49	0.012 18
4971.645 302	1800	−2.678 21	0.021 01
4972.672 436	1800	−2.561 29	0.013 19
4973.515 713	1800	−2.586 76	0.012 69
4974.678 659	1800	−2.714 13	0.013 59
4975.537 940	1800	−2.666 95	0.013 84
4976.683 662	1800	−2.555 67	0.013 04
4982.619 435	1800	−2.664 48	0.020 96
4983.621 314	1800	−2.567 77	0.014 86
4983.644 577	1800	−2.596 98	0.014 50
4984.578 450	1800	−2.558 37	0.014 74
4985.609 967	1800	−2.699 05	0.011 89
4995.555 496	1800	−2.508 58	0.013 96
5009.628 712	1800	−2.605 64	0.018 23
5010.596 729	1800	−2.538 71	0.023 13

Table B5. Radial velocity data for WASP-25 obtained using the HARPS high-precision echelle spectrograph. The point denoted by * was omitted from the analysis (see text for details).

HJD (−245 0000)	t_{exp} (s)	RV (km s^{-1})	σ_{RV} (km s^{-1})
5296.540 546	1200	−2.546 61	0.003 29
5296.635 060	1200	−2.543 81	0.003 98
5297.506 446	1200	−2.614 64	0.005 09
5297.518 749	400	−2.625 31	0.010 07
5297.523 714	400	−2.633 25	0.009 42
5297.528 714	400	−2.608 98	0.010 12
5297.533 807	400	−2.610 31	0.010 41
5297.538 714	400	−2.608 09	0.009 99
5297.543 714	400	−2.599 73	0.010 56
5297.548 668	400	−2.593 27	0.011 08
5297.553 761	400	−2.589 84	0.010 28
5297.559 131	400	−2.611 40	0.017 86
5297.563 761	400	−2.601 08	0.011 77
5297.568 668	400	−2.609 27	0.010 87
5297.573 715	400	−2.605 39	0.010 75
5297.578 761	400	−2.629 64	0.011 53
5297.583 668	400	−2.627 03	0.011 18
5297.588 669	400	−2.615 84	0.012 25
5297.593 715	400	−2.641 41	0.011 90
5297.598 669	400	−2.646 58	0.012 32

Table B5 – *continued*

HJD (−245 0000)	t_{exp} (s)	RV (km s^{-1})	σ_{RV} (km s^{-1})
5297.603 715	400	−2.657 55	0.012 34
5297.608 715	400	−2.675 20	0.012 46
5297.613 761	400	−2.675 58	0.012 54
5297.618 715	400	−2.685 67	0.012 44
5297.623 669*	400	−2.636 35	0.012 15
5297.628 854	400	−2.674 50	0.010 65
5297.633 761	400	−2.653 89	0.008 37
5297.638 715	400	−2.630 22	0.008 40
5297.643 773	400	−2.631 26	0.008 85
5297.648 727	400	−2.617 68	0.008 71
5297.653 727	400	−2.631 57	0.008 62
5297.658 681	400	−2.639 82	0.008 41
5297.663 773	400	−2.623 71	0.008 34
5297.668 773	400	−2.637 76	0.008 00
5297.673 727	400	−2.647 16	0.008 11
5297.678 727	400	−2.637 53	0.007 80
5297.683 681	400	−2.639 15	0.007 81
5297.688 820	400	−2.638 18	0.008 23
5297.693 727	400	−2.642 95	0.007 63
5297.698 774	400	−2.628 70	0.007 72
5297.703 635	400	−2.636 67	0.007 57
5297.708 727	400	−2.636 67	0.007 81
5297.713 727	400	−2.630 31	0.008 03
5297.718 681	400	−2.651 68	0.007 56
5297.723 774	400	−2.645 33	0.007 85
5297.833 578	1200	−2.656 76	0.003 52
5298.535 157	1200	−2.696 08	0.004 06
5298.716 015	1200	−2.691 19	0.002 85
5298.830 796	1200	−2.691 07	0.002 87
5299.544 943	1200	−2.606 03	0.003 27
5299.701 761	1200	−2.629 22	0.018 42
5299.838 220	1384	−2.575 73	0.012 24

Table B6. Radial velocity data for WASP-31 obtained using the CORALIE high-precision echelle spectrograph.

HJD (−245 0000)	t_{exp} (s)	RV (km s^{-1})	σ_{RV} (km s^{-1})
4835.809 755	1800	−0.202 60	0.029 45
4837.773 728	1800	−0.084 57	0.031 63
4840.765 776	1800	−0.079 74	0.037 52
4880.767 231	1800	−0.206 51	0.037 22
4939.627 676	1800	−0.075 28	0.034 71
4941.567 460	1800	−0.193 72	0.027 21
4942.654 757	1800	−0.123 24	0.025 98
4943.610 624	1800	−0.079 39	0.034 35
4944.555 415	1800	−0.165 78	0.026 20
4945.544 750	1800	−0.161 58	0.032 20
4946.591 778	1800	−0.044 22	0.034 41
4947.555 094	1800	−0.140 75	0.026 56
4948.588 069	1800	−0.182 74	0.028 61
4950.597 039	1800	−0.086 67	0.030 09
4951.608 264	1800	−0.228 21	0.033 66
4971.548 671	1800	−0.028 06	0.077 63
4973.489 951	1800	−0.091 89	0.030 84
4974.608 541	1800	−0.021 30	0.032 25
4975.511 060	1800	−0.126 28	0.033 81

Table B6 – *continued*

HJD (−245 0000)	t_{exp} (s)	RV (km s^{-1})	σ_{RV} (km s^{-1})
4983.595 539	1800	−0.100 28	0.044 15
4984.467 744	1800	−0.061 12	0.028 95
4985.530 406	1800	−0.188 86	0.030 32
4994.508 045	1800	−0.097 35	0.032 37
4994.531 307	1800	−0.094 84	0.034 69
4995.463 376	1800	−0.122 46	0.035 47
4995.486 741	1800	−0.209 99	0.032 14
4996.459 605	1800	−0.190 34	0.034 72
4996.482 971	1800	−0.109 84	0.031 17
4999.536 757	1800	−0.219 80	0.055 22
4999.560 099	1800	−0.156 70	0.065 60
5006.521 354	1800	−0.184 93	0.042 17
5012.492 297	1800	−0.096 67	0.037 39
5013.497 045	1800	−0.190 82	0.044 59
5029.465 780	1800	−0.116 60	0.050 41
5168.846 768	1800	−0.153 89	0.018 52
5203.782 854	2700	−0.201 52	0.020 84
5290.715 577	2700	−0.093 51	0.018 09
5291.699 859	2700	−0.122 73	0.018 21
5293.696 819	2700	−0.074 55	0.019 87
5294.733 907	2700	−0.097 85	0.019 25
5296.704 921	2700	−0.131 68	0.017 72
5298.693 406	2700	−0.182 10	0.017 18
5300.589 643	2700	−0.067 06	0.022 50
5326.628 560	2700	−0.138 31	0.019 45
5327.604 475	2700	−0.080 93	0.027 37
5328.608 442	2700	−0.099 12	0.019 13
5334.544 675	2700	−0.055 71	0.021 29

Table B7. Radial velocity data for WASP-31 obtained using the HARPS high-precision echelle spectrograph.

HJD (−245 0000)	t_{exp} (s)	RV (km s^{-1})	σ_{RV} (km s^{-1})
5298.496 133	1200	−0.156 38	0.008 96
5298.749 145	1200	−0.172 18	0.009 31
5299.504 441	1200	−0.171 41	0.011 14
5299.716 991	1200	−0.295 41	0.048 00
5300.509 357	1200	−0.079 10	0.011 38
5300.742 948	1200	−0.085 87	0.011 61
5301.582 822	1200	−0.115 16	0.009 34
5301.597 544	1200	−0.112 50	0.010 03
5301.612 960	1200	−0.125 27	0.009 84
5301.627 126	900	−0.108 41	0.014 18
5301.638 028	900	−0.093 94	0.011 41
5301.648 803	900	−0.063 09	0.012 27
5301.659 393	900	−0.087 76	0.011 00
5301.670 307	900	−0.113 21	0.011 36
5301.681 082	900	−0.135 42	0.011 19
5301.691 973	900	−0.167 17	0.012 18
5301.702 354	900	−0.195 79	0.012 97
5301.713 349	900	−0.167 96	0.014 07
5301.723 522	900	−0.161 42	0.018 84
5301.734 934	900	−0.146 95	0.017 71
5301.750 477	1200	−0.133 78	0.012 44
5301.764 794	1200	−0.140 88	0.015 86
5301.780 360	1200	−0.150 31	0.017 38
5305.613 529	1200	−0.181 66	0.010 96
5307.584 640	1200	−0.064 75	0.008 09

This paper has been typeset from a TEX/LATEX file prepared by the author.